Propagation and deposition of non-circular finite release particle-laden currents

Nadim Zgheib,[1,2] Thomas Bonometti,[2] and S. Balachandar[1,a)]
[1]*Department of Mechanical and Aerospace Engineering, University of Florida, Gainesville, Florida 32611, USA*
[2]*Université de Toulouse, INPT, UPS, IMFT, UMR 5502, Allée Camille Soula, F-31400 Toulouse, France*

The dynamics of non-axisymmetric turbidity currents is considered here for a range of Reynolds numbers of O (10^4) when based on the initial height of the release. The study comprises a series of experiments and highly resolved simulations for which a finite volume of particle-laden solution is released into fresh water. A mixture of water and polystyrene particles of mean diameter $\tilde{d}_p = 300$ μm and mixture density $\tilde{\rho}_c = 1012$ kg/m^3 is initially confined in a hollow cylinder at the centre of a large tank filled with fresh water. Cylinders with two different cross-sectional shapes, but equal cross-sectional areas, are examined: a circle and a rounded rectangle in which the sharp corners are smoothened. The time evolution of the front is recorded as well as the spatial distribution of the thickness of the final deposit via the use of a laser triangulation technique. The dynamics of the front and final deposits are significantly influenced by the initial geometry, displaying substantial azimuthal variation especially for the rectangular case where the current extends farther and deposits more particles along the initial minor axis of the rectangular cross section. Several parameters are varied to assess the dependence on the settling velocity, initial height aspect ratio, and volume fraction. Even though resuspension is not taken into account in our simulations, good agreement with experiments indicates that it does not play an important role in the front dynamics, in terms of velocity and extent of the current. However, wall shear stress measurements show that incipient motion of particles and particle transport along the bed are likely to occur in the body of the current and should be accounted to properly capture the final deposition profile of particles.

I. INTRODUCTION

When two fluids of different densities are brought into contact with one another (where the contact surface is parallel to the gravitational field), a hydrostatic pressure discontinuity forms along the interface and acts to set both fluids in motion. This type of fluid flow denoted as a gravity current[1,2] generally corresponds to the heavier of the two fluids intruding horizontally (normal to the gravitational field) into the lighter fluid. If we consider a laboratory setup in which both fluids are bounded by the impermeable walls of a finite domain (a tank, for example), then the lighter fluid simultaneously moves to occupy the space abandoned by the heavier fluid. The initial density jump across the interface need not be large; in fact, even a small density difference between the two Newtonian fluids is sufficient to generate a flow. Provided the length scale of the release (the height of the release) is large, the resulting flow will be sufficiently strong and turbulent. The density difference can arise from a number of scenarios including temperature, concentration, or

a)Author to whom correspondence should be addressed. Electronic mail: bala1s@ufl.edu. Telephone: (352) 392-8909. Fax: (352) 392-1071.

compositional disparities between the two fluids.[3] Here, we are interested in flows in which the density difference originates from the suspension of relatively dense particles. These types of currents are known as particle-laden flows[4–9] and constitute a more complex subset of gravity currents. The added complexity comes from the fact that the density of the current strongly depends on the volume fraction of suspended particles which is spatially and temporally dependent since particles may (i) settle out and deposit on the floor, (ii) roll, slide, or saltate along the bottom wall, or (iii) be reentrained back into the current if the latter is energetic enough. Furthermore, particle-laden flows may be longitudinally and/or vertically stratified in both grain size and concentration.[10]

For the case of spherical particles, the speed at which particles settle out is often taken to be the terminal velocity of a free-falling single particle.[11,12] The problems of bedload transport[13,14] and particle resuspension[15] are essentially non-linear, with difficulties arising from the randomness of turbulent fluctuations and the complex topography of the bed.[16]

Fixed volume, particle-laden flows are primarily investigated in one of two canonical configurations, namely, a planar setting[11,17] and a circular axisymmetric setting.[18–20] These works were mostly experimental and theoretical. Problems such as bedload transport and particle resuspension are often difficult to measure experimentally and therefore results from complementary direct numerical simulations (DNSs) are of value. Particle-laden currents which do not fall under these two canonical configurations remain largely unaddressed; the reason being that many natural configurations can be, to leading order, approximated as planar or axisymmetric, using geometrical arguments. The motivation behind the present work is to shed some light on the dynamics of particle-laden releases that are initially non-axisymmetric and non-planar and to highlight the importance of the details of the initial release. Such situations may occur, for example, in the dredging process where some sediment is intended to be deposited at some specific location which may depend on the initial shape of the release, or from voluntary or accidental collapse of buildings, the shape of which can influence the propagation and deposition of the debris. In the present work, we observe the short and long term dynamics of a non-canonical release (which is neither planar nor axisymmetric) to be dependent on the initial shape of the release.

Density-driven, finite-release saline currents with non-circular cross sections have been recently studied in Refs. 21 and 22. These authors showed that the dynamics of a gravity current is influenced by the initial shape of the release for the duration of the slumping and the inertia-buoyancy regimes. The proposed mechanism for the non-axisymmetric spreading of initially non-axisymmetric gravity currents is that during the acceleration and early part of the slumping phases, the initial release partitions itself into local volumes along the front, this partitioning being dictated by inward propagating geometric rays normal to the front. The subsequent outward propagation of the front is then dictated by these local volumes (in particular, the local height of the front) along the direction locally normal to the front. Experiments and DNS of saline rounded rectangular (non-axisymmetric) releases have shown that the resulting current reaches a self-similar spreading phase in which the temporally and azimuthally dependent front position $r_N(\theta,t)$, front velocity $u_N(\theta,t)$, and maximum height in the head of the current $h_N(\theta,t)$ may be expressed as

$$r_N(\theta,t) = R_N(t)\, f(\theta), \tag{1}$$

$$u_N(\theta,t) = \frac{dR_N}{dt} f(\theta) = U_N(t)\, f(\theta), \tag{2}$$

$$h_N(\theta,t) = H_N(t)\, f(\theta), \tag{3}$$

where $f(\theta)$ represents the self-similar shape of the front and R_N, U_N, and H_N may be expressed as power-laws, viz,

$$R_N(t) \propto t^{1+\alpha}, \quad U_N(t) \propto t^{\alpha}, \quad \text{and} \quad H_N(t) \propto t^{2\alpha}, \tag{4}$$

where the power-law exponent takes the value $\alpha = -1/2$. Furthermore, using an extended box model,[21] a scaling relation between the initial χ_0 and the self-similar χ_∞ horizontal aspect ratios of the rectangular cross section was proposed. Our aim here is to explore the case of particle-laden non-axisymmetric currents and in particular the azimuthal dependence of the initial non-circular shape on the velocity and extent of the current as well as the depositional pattern.

Direct numerical simulations of finite-release particle-laden flows have been performed for planar currents[23,24] but not for cylindrical releases. DNS allows exploration of local near-wall dynamics, specifically the bed shear stress and the near-wall velocity, both of which are critical quantities in the problems of bedload transport and particle resuspension. In addition, one can investigate the correlation of bed shear stress to the larger scale vortical structures.

In this paper, we perform a series of experiments of finite-volume, Boussinesq, particle-laden, and density-driven (scalar) flows. Cylinders with two different cross-sectional shapes are considered: a circle and a rounded rectangle (RR). For each experiment, we monitor the temporal evolution of the front as well as the final deposition profile of particles, both of which are highly dependent on the initial shape of release, as will be shown later. We vary several parameters, namely, the settling velocity, the initial height aspect ratio of the release, and the initial particle volume fraction, and analyze their influence on the current dynamics (front temporal evolution and deposition profile).

Companion direct numerical simulations are performed in which the setup is identical to that of the experiments. In our simulations, we do not account for particle resuspension or bedload transport. These assumptions will be discussed through the analysis of the spatial and temporal development of the wall shear stress and the near-wall fluctuating vertical velocity component inside the particle-laden flow.

Our paper is structured as follows. In Sec. II, we discuss the setup, procedure, and results of the experiments. In particular, we investigate the effects of the various parameters on the front velocity and deposition profiles. Direct numerical simulations are described in Sec. III and compared to experimental results. In particular, a possible mechanism for the switching of axes is provided in Sec. III E. The simplifications regarding bedload transport and particle resuspension are discussed in Secs. III F and III G, respectively. Conclusions are drawn in Sec. IV.

II. EXPERIMENTS OF FINITE-RELEASE NON-CIRCULAR PARTICLE-LADEN CURRENTS

A. Experimental setup

A particle-laden solution is confined within a hollow cylinder placed at the centre of a transparent glass square tank. The tank cross section is $\tilde{L}_x \times \tilde{L}_y = 120 \times 120$ cm and its walls are

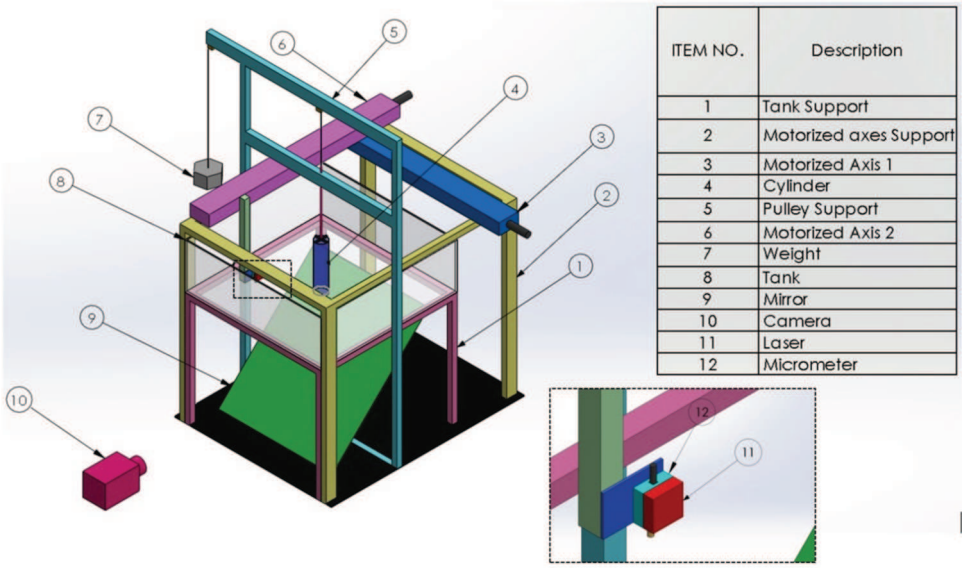

FIG. 1. Isometric view of the experimental setup. Inset: close-up view of the apparatus used to measure the deposit height. Note that for clarity, the tank and the motorized axes support have been removed from the picture in the inset.

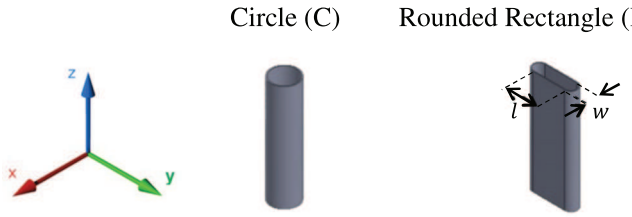

FIG. 2. Shape of the hollow cylinders used in the experiments. The height and equivalent radius of each cylinder are 400 mm and 46 mm, respectively. The size of the longest (shortest) side of the RR cylinder is 167 (44) mm. The length and width of the straight portion of the RR are denoted by $l = 123$ mm and $w = 44$ mm, respectively. Note that the horizontal cross section area is similar for both cylinders.

$\tilde{L}_z = 40$ cm high (see Figure 1). We consider two cross-sectional shapes for the hollow cylinder of height $\tilde{h}_0$ and equivalent radius $\tilde{R}_0$, the dimensions of which are given in Figure 2. The initial mixture, confined within the cylinder, is prepared by suspending polystyrene particles of density $\tilde{\rho}_p = 1050$ kg/m^3 and volume fraction ϕ_0 in tap water (here, tilde denotes a dimensional quantity). Particles are selected from a set of polydispersed particles, the granular size distribution of which being presented in Figure 3, using two sieves allowing to keep particles of diameters ranging in $[\tilde{d}_{min} = 280\ \mu\text{m}, \tilde{d}_{max} = 320\ \mu\text{m}]$. From Figure 3, it is reasonable to assume that the size of the selected particles is uniformly distributed in the range $[\tilde{d}_{min}, \tilde{d}_{max}]$ so that we may define the mean diameter as $\tilde{d}_p = (\tilde{d}_{min} + \tilde{d}_{max})/2 = 300\ \mu$m with a range of variability of $\pm 20\ \mu$m. It is noteworthy that the variation of the particle size around the mean diameter is about 7%, which is large enough to prevent the occurrence of crystallization and small enough insomuch as possible effects of segregation are likely to be weak when particles get concentrated at the bottom wall as they deposit.

Initially, a fixed quantity of particles of mass $\tilde{m}_p$ is poured into the hollow cylinder and both the tank and the cylinder are slowly filled with tap water ($\tilde{\rho}_a = 998$ kg/m^3). Once the desired level $\tilde{h}_0$ is reached, the water is given time to arrive at a stagnant state. As a precaution against the clustering of particles, a few drops of non-agglomerating solution are added to the mixture in addition to a fluorescent dye for visualization purposes. To bring the particles into suspension, two approaches were considered. In the first approach, a metallic net attached to a shape-fitted rigid structure that conforms to the inner perimeter of the hollow cylinder is used. The rigid structure is manually oscillated up and down within the hollow cylinder via two vertical rods that are connected to the structure at opposite ends. In the second approach, a brush of dimensions 4×1 cm connected at its end with a rigid metallic rod sweeps the bottom floor inside the cylinder. The latter of the two approaches was found to be more effective at suspending the particles and was adopted for all the experiments shown herein.

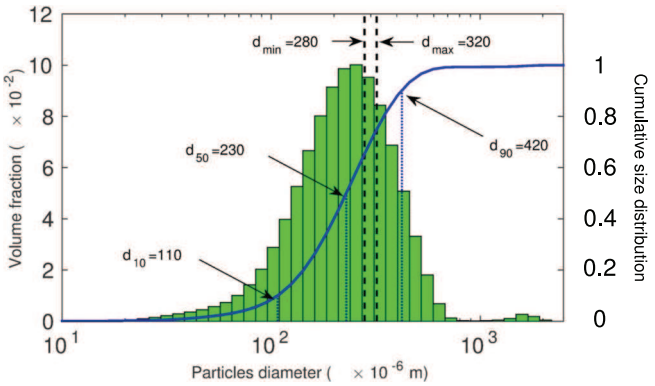

FIG. 3. Size distribution of the initial set of polystyrene particles used in the experiments (vertical bars: size distribution; solid line: cumulative size distribution). Note that the particles were selected in the range of diameters $[\tilde{d}_{min} = 280\ \mu\text{m}, \tilde{d}_{max} = 320\ \mu\text{m}]$ using sieves (dashed lines). Here, we define the mean diameter as $\tilde{d}_p = (\tilde{d}_{\min} + \tilde{d}_{\max})/2 = 300 \pm 20\ \mu$m.

B. Procedure

When the particles are fully suspended, the brush is retracted and the hollow cylinder is swiftly lifted via a pulley system (see Figure 1). To allow for a plan view of the current, a mirror at a 45° inclination is placed below the bottom transparent surface of the tank. A camera (sCMOS LaVision®, 2560×2160 pixels, 50 frames/s) points towards the centre of the mirror at a distance of 6 m. The experiments are carried out in a dark room with black light illuminating the fluorescent dye injected into the mixture. Neon black light tubes are mounted on the four sides of the tank with close proximity to the bottom surface where the turbidity current spreads.

Two sets of data are extracted: the temporal front evolution of the current, as well as the final thickness of the deposit, once the current arrives at a standstill. To capture the location of the front, high resolution (2160×2560 pixels) 16-bit grayscale images are recorded every 20 ms. The front can be readily discerned since there is an order of magnitude jump between intensity levels in just a few pixels at the current-ambient interface. The height of the deposited particles is measured at the end of each experiment with a non-intrusive technique through laser reflection, the basic principle of which is triangulation. The probe has two main optical elements. The first is a light emitting diode, which projects a visible laser beam on the surface of the targeted element (in this case, the deposit) whose elevation needs to be measured. A part of the incident beam is reflected from the surface of the deposit and impacts an ultra-sensitive optical sensor at an angle dependent on the distance between the diode and the surface. Before any experiments, calibration is performed, i.e., the elevation of the light emitting diode from the bottom surface of the tank is measured. Hence, once the distance between the diode and the targeted surface is measured, the height of the deposit can be straightforwardly obtained. The laser has a measuring range of 2 mm with a resolution of 0.5 μm and a spot diameter of 0.1 mm. The measurements are continuous with a frequency of 5 kHz. The 2 mm measuring range begins at a distance of 23 mm from the laser. The laser is an optoNCDT 1607 model manufactured by the German company MICRO-EPSILON. Since the surface of the deposit is not smooth, the readings of the laser typically fluctuate about a mean value. The magnitude of these fluctuations typically ranged between 50 and 100 μm and the maximum value remained below 200 μm. This maximum value was chosen as an estimate for the error. It is noteworthy that this value is less than the mean diameter of the particles (recall that $\tilde{d}_p = 300$ μm).

A mounted 2-axes motorized system is used to guide the laser over the bottom surface of the deposit. The system covers a range of 800×800 mm and depending on the area of the final deposit, the height of the particle deposit is measured every 25 or 50 mm. Since the height of the deposit at the centre of the release can exceed the aforementioned 2 mm measuring range, a micrometre was attached to the laser (see the inset of Figure 1) to allow for controlled vertical displacements.

To account for slight possible inclination in the tank supporting structure or possible minute height variations caused by the bending of the motorized axis (due to its own weight) as the laser sweeps over the bottom surface, dry measurements of the tank "topography" were computed by displacing a metallic plate of known thickness at various locations in the tank and recording the elevation measured by the laser. These values are then taken into account to correct the final thickness of the deposit.

As an attempt to assess the accuracy of the beam measurements, we enclose a known mass of particles within a cylinder (open at one end) of known diameter, $D_c = 84$ mm. After the elevation δ_0 of the bottom plate of the cylinder was measured, a mass $M_1 = 18$ g of particles was placed inside the cylinder. The cylinder was then gently shaken so that the particles were uniformly distributed within it. The elevation δ_1 of the particles was then recorded at multiple locations. We repeated the measurements for $M_2 = 26$ g and $M_3 = 34$ g and the corresponding elevations δ_2 and δ_3 were recorded. From a mass M_i, density ρ_p, and compactness factor C, the elevation δ_i of particles within a cylinder of diameter D_c may be estimated as

$$\delta_i = \frac{M_i}{\rho_p C(\pi D_c^2/4)}. \tag{5}$$

Here, the compactness factor C was chosen to correspond to loose randomly packed spheres, i.e., $C = 0.6$ approximately.[25] The discrepancy between the measured and expected values was found to be in the range of 3%–7%.

Since the laser cannot be immersed in water and because of the close proximity required between the laser and the deposit, the tank is slowly emptied at the end of each experiment and the deposit is allowed to dry overnight before any measurements are undertaken. The thickness is recorded at multiple height levels of the laser apparatus to ensure that the surface of the deposit always lies in the 2 mm measuring range of the laser.

C. Results

1. Evolution in the horizontal (x, y)-plane

Various experiments were carried out in order to assess the dependence of the dynamics on the initial volume fraction ϕ_0, initial height aspect ratio λ, and settling velocity $\tilde{V}_s$. Here, the initial volume fraction ϕ_0 is the ratio of the volume occupied by the particles to the total volume of the mixture at the time of release and λ is defined as the initial height $\tilde{h}_0$ of the mixture inside the cylinder divided by the equivalent radius $\tilde{R}_0$ of the cylinder ($\lambda = \tilde{h}_0/\tilde{R}_0$). Unless stated otherwise, all variables are scaled by the following characteristic length, velocity and time, respectively, viz,

$$\tilde{L} = \tilde{h}_0, \quad \tilde{U} = \sqrt{\tilde{g}\frac{\tilde{\rho}_{c0} - \tilde{\rho}_a}{\tilde{\rho}_a}\tilde{h}_0}, \quad \tilde{T} = \frac{\tilde{L}}{\tilde{U}}, \tag{6}$$

where $\tilde{g}$ is the gravitational acceleration, $\tilde{\rho}_{c0}$ is the initial equivalent density of the mixture, and $\tilde{\rho}_a$ is the density of the ambient fluid. In practice, the initial density of the mixture is computed as $\tilde{\rho}_{c0} = \phi_0\tilde{\rho}_p + (1 - \phi_0)\tilde{\rho}_a$, where $\tilde{\rho}_p$ is the density of the particles.

A list of the experiments is shown in Table I. Note that the shape refers to the cross-sectional outline of the hollow cylinder, with RR denoting the rounded rectangular cylinder and C signifying a circular cylinder. Both geometries were chosen to have similar cross-sectional areas of 68 and 69 cm^2 for the circular and rounded rectangular cross sections, respectively. Therefore, for a fixed initial height, the volume of the release for the rounded rectangle and the circular cylinder is nearly equal. We follow[26] by defining the settling velocity $\tilde{V}_s$ of the particles as

$$\tilde{V}_s = \tilde{\tau}\,(1 - \beta)\,\tilde{g}, \tag{7}$$

TABLE I. List of experiments. RR, rounded-rectangle; C, circle; *Re*, Reynolds number defined in (9); $\lambda = \tilde{h}_0/\tilde{R}_0$, initial height aspect ratio with $\tilde{h}_0$ being the initial height of the mixture inside the cylinder and $\tilde{R}_0$ the equivalent radius of the cylinder; $\tilde{\rho}_{c0}$, initial density of the mixture; $\tilde{m}_p$, initial mass of particles; ϕ_0, initial volume fraction; $\tilde{d}_p$, mean particle diameter; and V_s, dimensionless settling velocity.

Experiment	Shape	*Re*	λ	$\tilde{\rho}_{c0}$ (kg/m^3)	$\tilde{m}_p$ (g)	ϕ_0	$\tilde{d}_p$ (μm)	V_s
1	RR	10 520	2	1012	180	0.27	300 ± 20	0.020
2	RR[a]	10 520	2	1012	180	0.27	300 ± 20	0.020
3	RR	3 720	1	1012	90	0.27	300 ± 20	0.029
4	RR[b]	3 720	1	1012	0	…	…	…
5	RR	3 720	1	1012	90	0.27	670 ± 40	0.11
6	RR	2 630	1	1005	45	0.13	300 ± 20	0.04
7	C	3 720	1	1012	90	0.27	300 ± 20	0.029
8	C[b]	3 720	1	1012	0	…	…	…
9	RR	1 315	0.5	1012	45	0.27	300 ± 20	0.04
10	C	10 520	2	1012	180	0.27	300 ± 20	0.020

[a]The experiment was done in a tank with narrower lateral boundaries.
[b]The experiment is for a saline current.

where

$$\tilde{\tau} = \frac{\tilde{d}_p^2(\hat{\rho} + 1/2)}{18\tilde{\nu}(1 + 0.15Re_p^{0.687})} \quad \text{and} \quad \beta = \frac{3}{2\hat{\rho} + 1}, \tag{8}$$

with $\hat{\rho} = \tilde{\rho}_p/\tilde{\rho}_a$ denoting the ratio of the particle density to the fluid density, $Re_p = \frac{\tilde{V}_s \tilde{d}_p}{\tilde{\nu}}$ representing the particle Reynolds number, and $\tilde{\nu}$, the kinematic viscosity of the interstitial fluid (water). Finally, the Reynolds number is defined as

$$Re = \frac{\tilde{h}_0 \tilde{U}}{\tilde{\nu}}. \tag{9}$$

We first explore the effect of the initial shape of the release on the temporal evolution of the front of a particle-laden current. Here, we investigate the finite-release of roughly monodisperse, particle-laden currents for a non-planar, non-axisymmetric geometry. Let us consider, for example, the rounded-rectangular release shown in Figure 4(b). Note that for comparison, we present the case of a circular release in Figure 4(a). Initially, the longest side of the rounded rectangle is parallel to the y-axis and once released, the front advances in all directions. The current is seen to attain a roughly circular cross section at $t = 10$. However, at later stages of spreading ($t > 10$), a difference between the spreading distances along the x and y-axes is observed. Clearly, the spreading is faster along the x-axis of the release. This preferred spreading direction is observed to persist until the current comes to rest at $t \approx 70$ (not shown). Note that from $t = 40$ to $t \approx 70$, the current advances at such a slow rate that its final layout is almost identical to that at $t = 40$.

As for the rounded-rectangular cross section, we define two specific axes, denoted as minor and major axes, which initially correspond to the direction of shorter and longer sides, respectively. In the present work, they are initially parallel to the x- and y-axes, respectively. In the following, we refer to the switching of axes when the current's major axis rotates by 90° (with respect to the centre of the release in the x-y plane) from the time it is released to the time when it arrives at a complete standstill. For the rectangular release displayed in Figure 4(b), the current is observed to switch axes (see snapshots at $t = 0$ and $t = 40$). Note that this switching of axes for this initial shape of release has been previously reported in the case of homogeneous saline currents.[21]

We plot in Figure 5 the mean front location at select instances for saline and particulate currents pertaining to experiments 3, 4, 7, and 8. Here, the front position which is plotted in the $(x \geq 0, y \geq 0)$-domain has been averaged in space using symmetry along the x- and y-axes, respectively. To be more explicit, we exploit the 4-fold symmetry in the x-y plane by first mapping all points along the front onto the first quadrant $(x \geq 0, y \geq 0)$. In practice, a point on the front with coordinates (x, y) gets the new coordinates $(|x|, |y|)$ that belong to the first quadrant. We then convert the Cartesian coordinates $(|x|, |y|)$ to polar coordinates (r, θ), with r being the radial distance from the origin to the point and θ being the angle made with respect to the x-axis $(0 \leq \theta \leq \pi/2)$. Subsequently, we average all the r values at each equally spaced θ in steps of $\pi/180$. The front of the saline current appears to be much smoother than that of the particle-laden current. The latter shows a fingering, lobe-and-cleft-like instability towards the later stages of the release (Figure 5, $t \geq 20$). This type of instability has been observed in particle-laden gravity currents flowing down an incline.[27] The mechanism leading to the formation of this lobe-and-cleft-like instability in a particulate current is not fully explored. References 18 and 23 have shown that for finite-volume axisymmetric and planar releases, homogeneous and particulate currents advance at similar speeds until enough particles have settled and particle-laden fronts begin to progressively slow down and deviate from scalar driven fronts. For the circular release (Figure 5(a)), we observe that the time of separation occurs after $t \approx 10$. Interestingly, for the rounded-rectangular release (Figure 5(b)), the time, from which deviation between saline and particulate fronts is observed, is azimuthally dependent. Until $t = 5$, both currents advance at the same rate. At $t = 10$, the particulate front overtakes the saline front along the x-axis, with the fronts progressively reuniting as we get closer to the y-axis. At later times ($t = 20$), the particle-laden front matches the saline front along the x-axis. Finally, at $t = 40$, the difference between the fronts grows, with a larger discrepancy along the y-axis.

We plot in Figure 6 the contour plots of the mean deposition thickness $\bar{h}_d$ of the current displayed in Figure 5. Here, $\bar{h}_d$ has been obtained by averaging the local deposition thickness over the

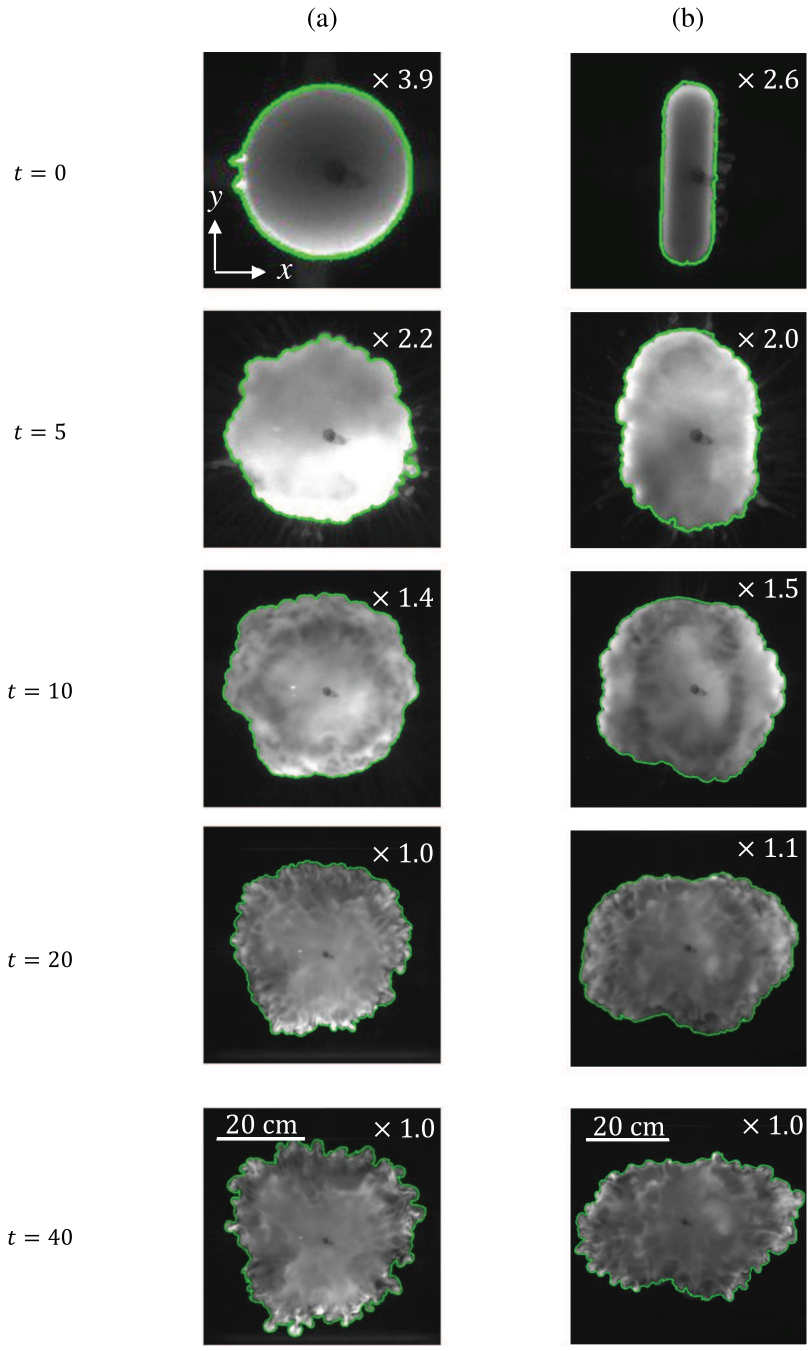

FIG. 4. Top view of the collapse of a turbidity current of initial (a) circular cross section (Exp 7) and (b) non-circular cross section (Exp 3). The detected front is plotted in green contour. The current in (b) is observed to switch axes between $t = 10$ and $t = 40$. All times are dimensionless. A separate scale bar is shown for each experiment at $t = 40$. The magnification factor on the top right of each image corresponds to its respective scale bar. Recall that one dimensionless unit corresponds to 93 mm.

four quadrants as

$$\bar{h}_d(x \geq 0, y \geq 0) = \frac{1}{4}(h_d(x, y) + h_d(-x, y) + h_d(x, -y) + h_d(-x, -y)). \tag{10}$$

The deposit of the circular release remains axisymmetric with regular spacing between contour levels indicating a uniform steady decline in the amount of deposit along the radial direction.

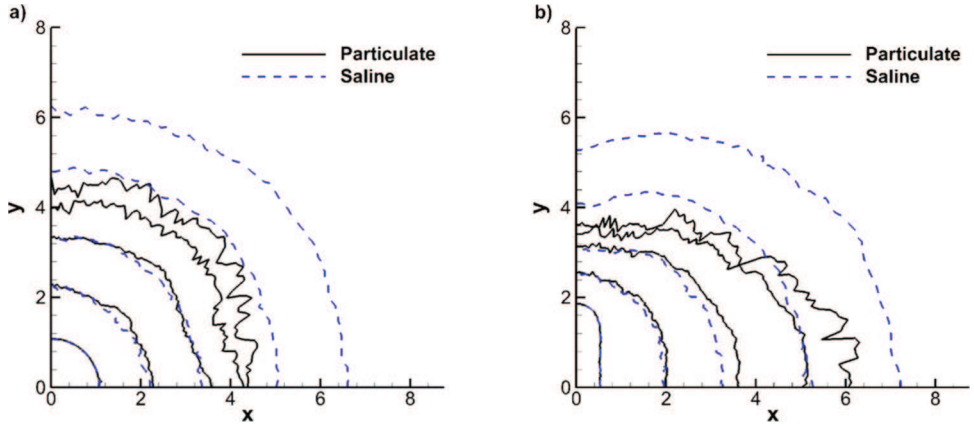

FIG. 5. Time evolution of the mean front location of a particulate (solid line) and saline (dashed line) current of initial (a) circular cross section (Exps 7 and 8) and (b) rounded-rectangle cross section (Exps 3 and 4). The fronts are shown at a dimensionless time of $t = 0$, 5, 10, 20, and 40.

Alternatively, for the rounded rectangular release, the contour lines spatially evolve from an initial rectangular-like outline conforming to the initial shape of the release to another rectangular-like outline, the longest side being aligned with the x-axis. In addition, the spacing between the contours is no longer uniform as in the circular case. For example, the distance between the contour $\bar{h}_d = 4 \times 10^{-2}$ and $\bar{h}_d = 2.5 \times 10^{-2}$ is 4 times larger along the x-axis as compared to the y-axis. Overall, Figure 6 shows that the final layout of the deposition profile is influenced by the initial shape of the release.

2. Evolution along the x- and y-axes

The dynamics and deposition of a finite-volume release of particle-laden currents are here shown to depend on the initial shape of the release. For the RR-geometry considered here, we identify two specific directions along which the variability in front position and amount of sedimentation is the most contrasted, namely, the so-called minor and major axes oriented along the x-axis and y-axis, respectively.

For the RR-geometry, the initial major axis corresponds to the slowest direction of spreading along which the current covers the smallest distance, whereas the initial minor axis corresponds to the fastest direction of spreading along which the current covers the largest distance. The time

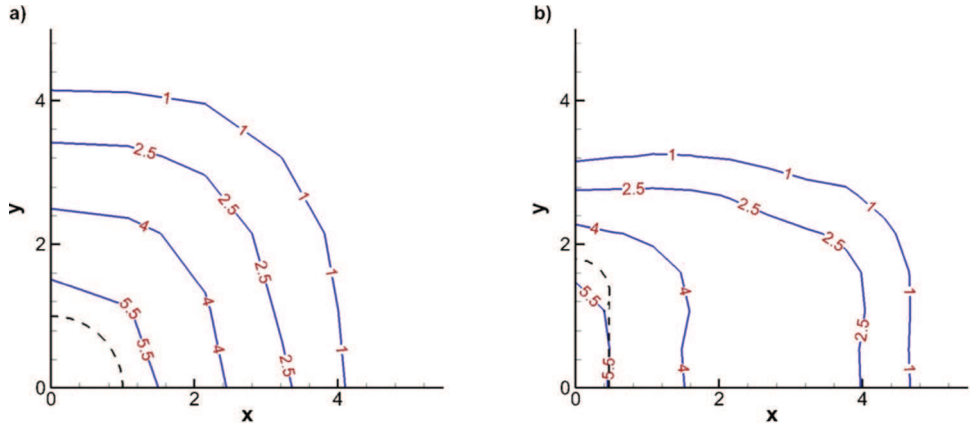

FIG. 6. Iso-contours of the dimensionless mean deposition thickness $\bar{h}_d$ of a turbidity current of initial (a) circular cross section (Exp 7) and (b) non-circular cross section (Exp 3). The dashed lines represent the boundaries of the hollow cylinders. Values of $\bar{h}_d$ are given in percent of the initial height of the release (i.e., the iso-contour values 1, 2.5, 4, and 5.5 correspond to a dimensionless deposition thickness of 0.01, 0.025, 0.04, and 0.055, respectively).

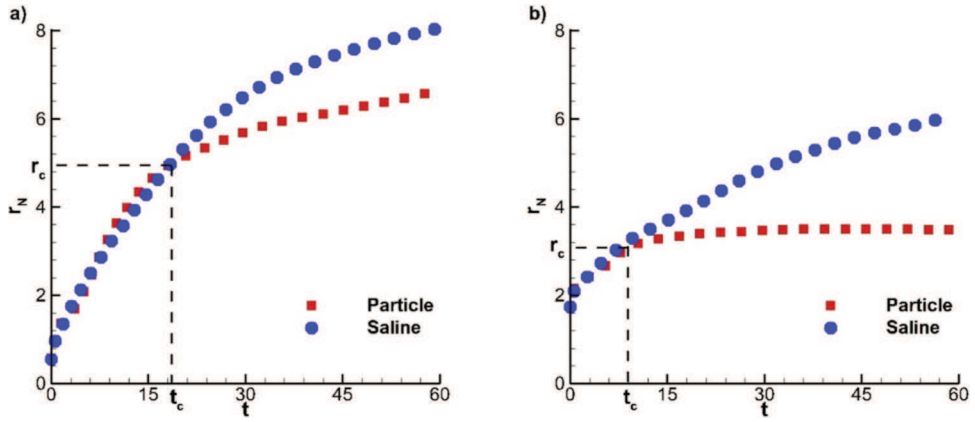

FIG. 7. Front position r_N versus time for the RR-turbidity current (Exp 3, squares) and the RR-saline current (Exp 4, circles) along (a) the minor x-axis and (b) the major y-axis. The vertical (horizontal) dashed line corresponds to the critical time t_c (location r_c) beyond which the saline front progressively deviates from the particle-laden front.

evolution of the front position along the minor x-axis and major y-axis of the RR-turbidity and the RR-saline currents is presented in Figure 7. The vertical dashed line indicates the time t_c beyond which the fronts continually deviate from one another as a result of particle sedimentation. Here, t_c is computed as the time from which

$$r_s > r_p \quad \text{and} \quad d(r_s - r_p)/dt > 0.02, \tag{11}$$

where r_s and r_p are the distances between the centre and the front of the saline and particulate currents, respectively. The time t_c is observed to be non-uniform along the front, but rather azimuthally dependent. The deviation between the saline-driven and particle-driven fronts is observed to first occur along the major axis $t_c \approx 9$. Along the minor axis, the fronts advance at the same rate for a longer time $t_c \approx 18$. Figure 7 shows that both saline and particulate currents exhibit a preferential spreading direction, which leads to the switching of major and minor axes.

In Figure 8, we present the mean deposition thickness $\bar{h}_d$ of the final deposit along the x- and y-axes. The deposition thickness along the y-axis sharply drops beyond $r = 1$. Along the x-axis, however, the variation in thickness is slower and the current has deposited particles over a distance of 10 times the corresponding lock length. Figures 7 and 8 indicate that the radial position of the front at time t_c is close to the location where the deposition thickness becomes negligible, say less

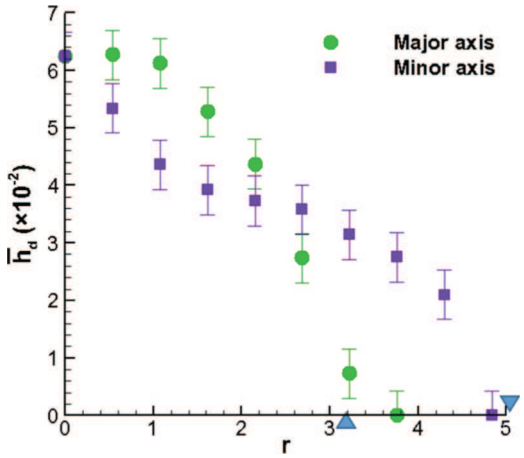

FIG. 8. Mean final deposition thickness $\bar{h}_d$ versus radial distance along the minor x-axis (squares) and major y-axis (circles) for the RR-turbidity current (Exp 3). The bars correspond to the measurement error. The upward (downward) triangles indicate the location of the critical radius of the front r_c along the minor (major) axis (see Figure 7 for details).

than a percent. This may suggest that the change in the dynamics between the turbidity current and the saline current at $t \approx t_c$ is due to the fact that most of the particles have sedimented and hence for $t > t_c$, the concentration of particles in the turbidity current is much smaller than ϕ_0, these particles being transported as a suspension. We do not have access in the experiments to the time evolution of the deposited sediments, but we may calculate from direct numerical simulations (discussed in Sec. III) the amount of particles remaining in suspension at $t = 9$ and $t = 18$, which correspond to t_c along the y and x axes, respectively. At $t = 9$, around 35% of particles remain in suspension, most of which (over 85%) however reside in two symmetric 90° wedges centred on the positive and negative x-axis (i.e., only a small portion of particle-laden mixture is available to the slow moving front along the y-axis). At $t = 18$, less than 10% of particles remain in suspension, most of which (~95%) are confined within two symmetric 90° wedges centred on the positive and negative x-axis.

3. Influence of the settling velocity

While the effect of varying the settling velocity (via particle diameter) has been investigated in the past for circular turbidity currents,[18] here we explore the configuration of non-circular geometries in Figure 9. In this section, we mainly consider Exps 3 ($V_s = 0.029$), 4 ($V_s = 0$), and 5 ($V_s = 0.11$). Note that Exp 4 is a saline current but here, it is regarded as a limiting case of a particle-laden current with zero settling velocity, while the mean particles diameter in Exp 5 is about twice as large as that in Exp 3. Note that the initial density of the current in these experiments is identical and hence, the currents are likely to advance at the same velocity at early times, as confirmed in Figure 9 showing the temporal evolution of the front position. Here, the effect of settling velocity is first perceived along the initial major axis, for which the front dynamics deviate from one experiment to the other at a much earlier time ($t \approx 3$). In the case $V_s = 0.11$, the current ceases to advance along the major axis at $t \approx 5$, while along the initial minor axis, the deviation occurs at $t \approx 6$. It is important to note that switching of axes is observed for all the cases considered in Figure 9. As for the deposition pattern, we observe that the larger V_s, the smaller the extent and hence the larger the thickness at the centre (not shown). For instance, $\bar{h}_d \approx 6 \times 10^{-2}$ at the centre of the deposit for $V_s = 0.029$ and $\bar{h}_d \approx 9 \times 10^{-2}$ at the centre of the deposit for $V_s = 0.11$. This is in line with the results of Figure 9 showing that the distance of propagation is smaller as V_s is increased, due to the stronger sedimentation process.

4. Influence of the initial volume fraction

In this section, we consider the effect of the initial volume fraction ϕ_0 by comparing the results of Exp 3 to those of Exp 6 for which $\phi_0 = 0.27$ and 0.13, respectively. Figure 10 shows the time

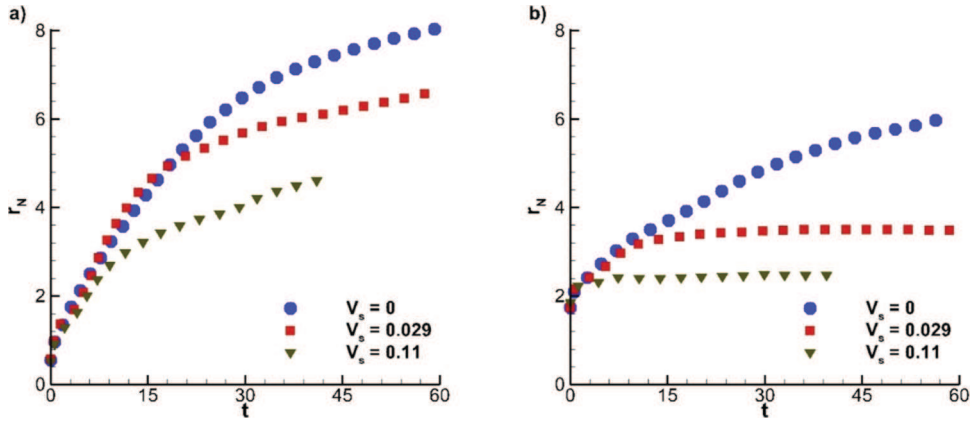

FIG. 9. Front position versus time for currents of various settling velocities V_s along (a) the minor x-axis and (b) the major y-axis: blue filled circle, $V_s = 0$ (Exp 4); red filled square, $V_s = 0.029$ (Exp 3); dark green inversed filled triangle, $V_s = 0.11$ (Exp 5).

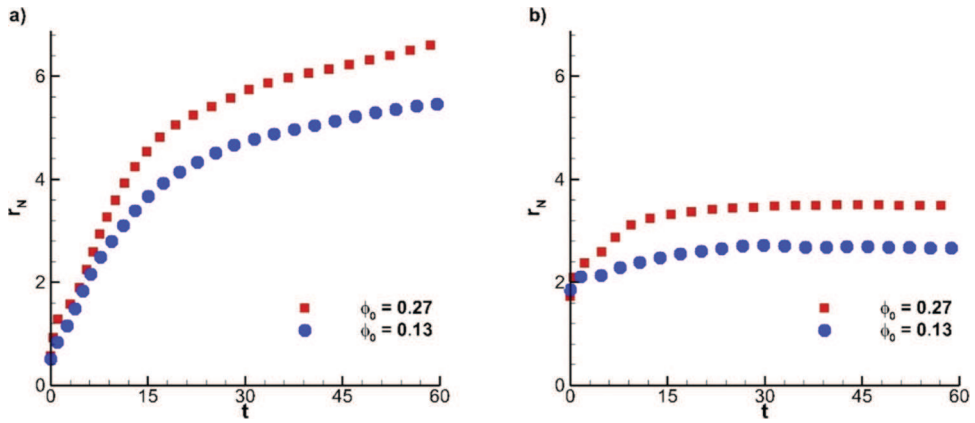

FIG. 10. Front position versus time for various initial volume fractions ϕ_0 along (a) the minor x-axis and (b) the major y-axis: blue filled circle, $\phi_0 = 0.13$ (Exp 6); red filled square, $\phi_0 = 0.27$ (Exp 3).

evolution of the front position along the x-axis and y-axis in both cases. We observe that with a smaller initial particle volume fraction, the extent of the front along the specific axes is smaller as well; however, the switching of axes is still identifiable. The smaller spreading distance in Exp 6, which is a result of the lower initial volume fraction, is observed to vary azimuthally since the propagation distance $(r_N - r_N(t = 0))$ is shorter by 50% along the major axis and by 20% along the minor axis, as compared to the propagation distance in Exp 3. The deposition profile of the $\phi_0 = 0.27$-current is somewhat similar to that of the $\phi_0 = 0.13$-current, as shown in Figure 11. A close inspection of the deposition patterns in both cases (see, e.g., Figures 6(b) and 11(a)) indicates that the extent of the deposit is slightly smaller in the case of the current of smaller initial volume fraction, as a result of the initial reduced gravity and hence smaller front speed.

5. *Influence of the initial height aspect ratio*

In order to investigate the influence of the initial height aspect ratio λ, we carried out three experiments where the geometry, volume fraction, and particle diameter were held constant. Three values of λ were chosen, namely, 0.5, 1, and 2 (corresponding to experiments 9, 3, and 1, respectively). In Figure 12, we compare the time evolution of the front position along the x- and y-axes. Note that for clarity, we choose a fixed length scale of $\tilde{h}_0 = 4.65$ cm pertaining to Exp 3. This

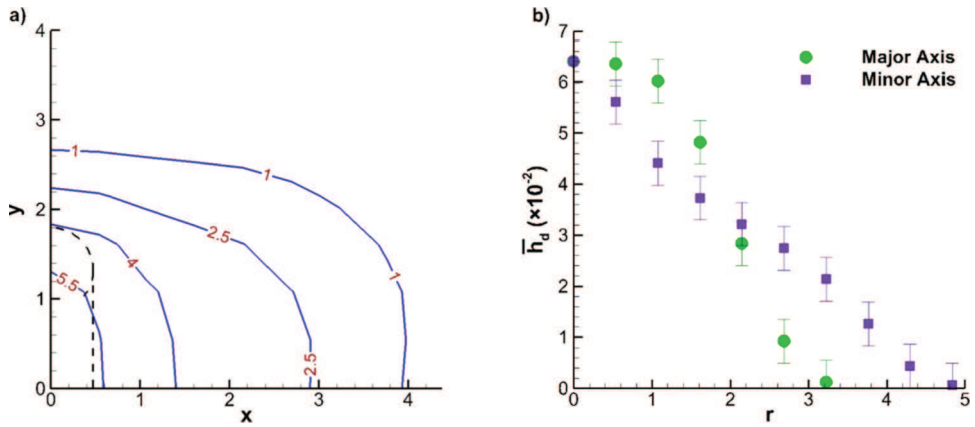

FIG. 11. (a) Iso-contours of the mean deposition thickness $\bar{h}_d$ of the $\phi_0 = 0.13$—turbidity current (Exp 6). The dashed line represents the boundaries of the hollow cylinder. (b) Corresponding mean final deposition thickness versus radial distance along the major y-axis (circles) and minor x-axis (squares). The bars correspond to the measurement error.

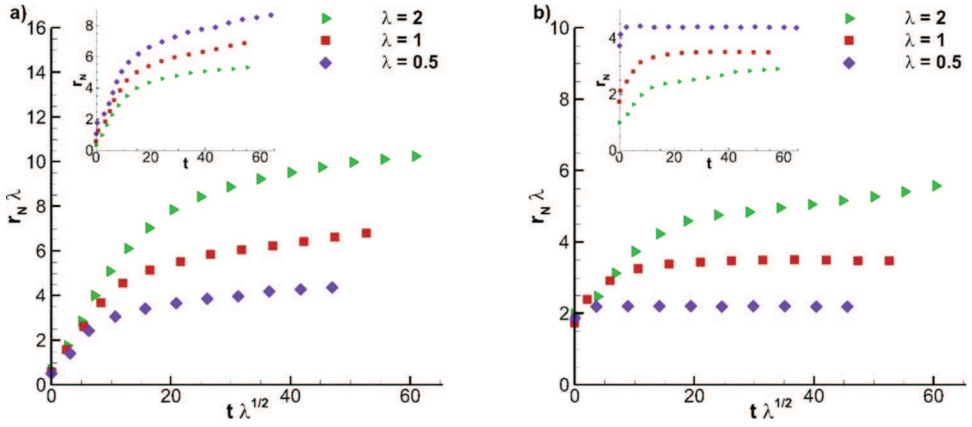

FIG. 12. Front position versus time for currents of various initial height aspect ratios λ along (a) the minor x-axis and (b) the major y-axis: purple filled diamond, $\lambda = 0.5$ (Exp 9); red filled square, $\lambda = 1$ (Exp 3); light green right faced filled triangle, $\lambda = 2$ (Exp 1).

is equivalent to plotting $r_N\lambda$ as a function of $t\sqrt{\lambda}$. For comparison, we plotted in insert r_N as a function of t. As the initial height aspect ratio is increased, the extent of the current is increased, as expected. For all λ, the current's dynamics is non-axisymmetric and we observe a switching of axes, the long-time length-to-width ratio remaining uniform with a value of 1.9, approximately.

The final mean deposition thickness along the minor and major axes is shown in Figure 13. First, as λ is increased, the thickness of the deposit at the centre of the release is observed to decrease (recall that we adopt a single length scale for all three experiments). Second, the slope of the deposition profile is lower (along both specific axes) as λ is increased. This indicates a stronger transport of the particles inside high-λ currents, which is in line with the fact that here the Reynolds number of the currents is larger at high λ (see Table I) and hence, the propagation is faster (in the range of Reynolds numbers considered here).

6. *Influence of the lateral boundaries*

In order to assess the influence of the tank boundaries on the dynamics of the currents, we performed an extra-experiment (Exp 2) where we placed 2 vertical panels (each at an opposite end of the tank) having the same width and height as the tank at a distance of 10 cm from the tank walls normal to the x-axis. With the panels in place, the new dimensions of the tank become

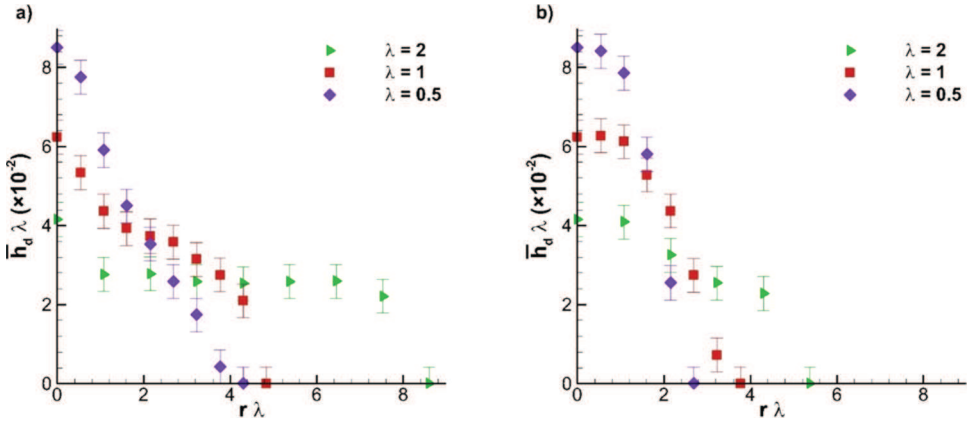

FIG. 13. Mean final deposition thickness $\bar{h}_d$ versus radial distance for various initial height aspect ratios λ along (a) the minor x-axis and (b) the major y-axis: purple filled diamond, $\lambda = 0.5$ (Exp 9); red filled square, $\lambda = 1$ (Exp 3); light green right faced filled triangle, $\lambda = 2$ (Exp 1). The bars correspond to the measurement error.

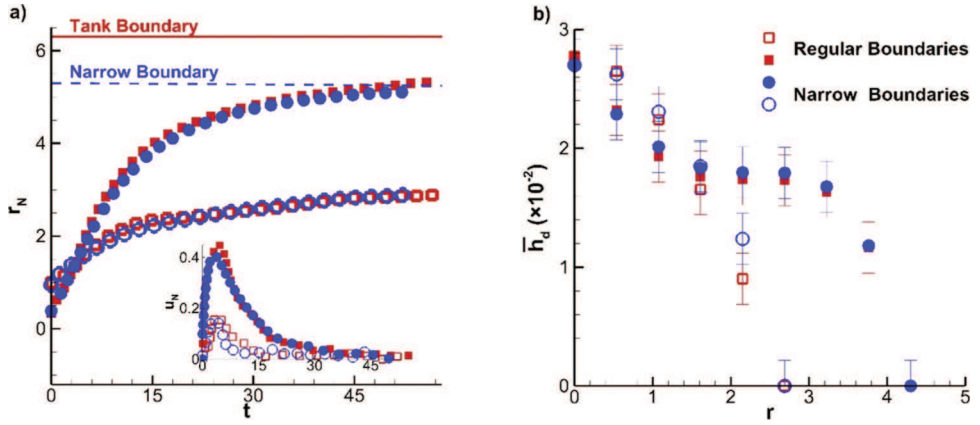

FIG. 14. (a) Front position versus time for Exp 1 (squares) and Exp 2 (circles) along the x (filled symbols) and y (hollow symbols) axes. The solid and dashed lines represent the location of the tank lateral wall in Exps 1 and 2, respectively. Inset: corresponding time evolution of the front velocity. (b) Corresponding mean final deposition thickness $\bar{h}_d$.

$\tilde{L}_x \times \tilde{L}_y \times \tilde{L}_z = (100 \times 120 \times 40)$ cm. In Figure 14, we present the temporal evolution of the front position r_N, front velocity u_N, and the final mean deposition thickness $\bar{h}_d$ along the x and y axes. The results indicate that the position of the boundaries does not hinder the advancement of the current or its deposition profile. Furthermore, from the inset of Figure 14(a), the front velocity (along the x-axis) is observed to drop down to 10 times its maximum value as the front advances beyond $t = 30$. Here, u_N is calculated through backward differencing from a high order polynomial curve fit of the front position. The large reduction in speed as the current approaches the boundaries is the primary reason for the marginal effect of the lateral boundaries on the current dynamics and particle deposition. Furthermore, the differences between experiments 1 and 2 in terms of r_N, u_N, and $\bar{h}_d$ are indicative of experimental uncertainties and remain smaller than the differences due to the non-axisymmetric nature of the release.

III. SIMULATIONS OF FINITE-RELEASE NON-CIRCULAR PARTICLE-LADEN CURRENTS

A. Equations and numerical setup

The particle-laden mixture is here treated as a continuum and a two-fluid formulation is adopted. We follow[28] by implementing an Eulerian-Eulerian model of the two-phase flow equations. The model involves mass and momentum conservation equations for the continuum fluid phase, an algebraic equation for the particle phase momentum, where the particle velocity is taken to be equal to the local fluid velocity and an imposed settling velocity derived from the Stokes drag force on the particles and a transport equation for the dimensionless particle phase concentration ρ. The dimensionless system of equations reads

$$\nabla \cdot \boldsymbol{u} = 0, \tag{12}$$

$$\frac{D\boldsymbol{u}}{dt} = \rho \boldsymbol{e}^g - \nabla \mathrm{p} + \frac{1}{Re}\nabla^2 \boldsymbol{u}, \tag{13}$$

$$\boldsymbol{u}_p = \boldsymbol{u} + V_s \boldsymbol{e}^g, \tag{14}$$

$$\frac{\partial \rho}{\partial t} + \nabla \cdot (\rho \boldsymbol{u}_p) = \frac{1}{Sc\,Re}\nabla^2 \rho. \tag{15}$$

We denote by $\boldsymbol{u}_p$ and $\boldsymbol{u}$ the velocities of the particle and continuum fluid phases, respectively. The settling velocity V_s is determined from the Stokes drag force on spherical particles with small particle Reynolds number as defined in (7). $\boldsymbol{e}^g$ is a unit vector pointing in the direction of gravity. Here, we employ the Boussinesq approximation assuming that small density differences between the particle-laden solution and the ambient play a role only in the buoyancy term (first term in the

R.H.S of (13)). Unless stated otherwise, all the parameters are dimensionless. The length, velocity, and time scales are identical to those defined in (6). The density and total pressure are made dimensionless as follows (recall that tilde denotes a dimensional quantity):

$$\rho = \frac{\tilde{\rho} - \tilde{\rho}_a}{\tilde{\rho}_{c0} - \tilde{\rho}_a}; \qquad p = \frac{\tilde{p}}{\tilde{\rho}_a \tilde{U}^2}. \tag{16}$$

The Schmidt number introduced in (15) represents the ratio of the diffusivities in the velocity and density fields. In the case of scalar density currents involving immiscible fluids (oil and water, for example), the Schmidt number is infinite. In the present case of particle-laden currents, the Schmidt number is a complex quantity that depends on effective particle diffusivity that arises from particle number density fluctuations. Here, the value of the Schmidt number is set to unity for simplicity. The value of the Schmidt number however only weakly influences the flow structure and dynamics in the case of high Reynolds number flows of order (10^4)[29] and thus its influence can be considered significant only in the very late stages of the spreading of the current.

The numerical setup depicted in Figure 15 is identical to that of the experiments. The simulations are carried out inside a rectangular computational domain of dimensions $L_x \times L_y \times L_z$ using a spectral code which has been extensively validated.[30,31] Periodic boundary conditions are imposed along the horizontal x- and y-directions. No-slip and free-slip conditions are imposed for the velocity of the continuous phase along the bottom ($z = 0$) and top ($z = 1$) walls, respectively. Mixed and Neumann boundary conditions are imposed for the concentration of the particle phase at the top and bottom walls, which translate into zero particle resuspension and zero particle net flux, respectively, viz,

$$\left(\frac{\partial \rho}{\partial z}\right)_{z=0} = 0; \quad \left(\frac{1}{Sc\,Re}\frac{\partial \rho}{\partial z} - V_s \rho\right)_{z=1} = 0. \tag{17}$$

Note that here the condition $\partial\rho/\partial z = 0$ at the bottom wall corresponds to a non-zero advective flux due to the sedimentation of the particles which, in the present case where resuspension is neglected, is a measure of the deposit.[26] We present results from the simulations listed in Table II. Note that simulation 1 (circular release) corresponds to Exp 10 while simulations 2 and 3 (rounded-rectangular release) correspond to Exp 1. The Reynolds number of all the simulations was set at $Re = 8430$, which is lower than that of the experiments ($Re = 10\,520$). The Reynolds number and grid resolution were chosen to achieve a range between 4 and 6 decades of decay in the energy spectrum for all variables. The reason about having two simulations for a single experiment is to assess a possible effect of turbulence initially present in the real system due to (i) initial stirring performed inside the hollow cylinder in order to create a homogeneous suspension before releasing the current and (ii) the shear at the walls of the hollow cylinder which is generated during lift off. On the one hand, the release mechanism may generate some large-scale vorticity and velocity

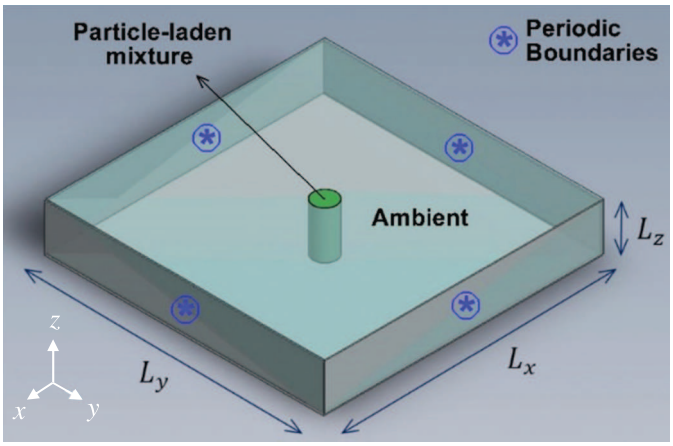

FIG. 15. Numerical setup.

TABLE II. List of simulations. RR, rounded-rectangle; C, circle; Re, Reynolds number defined in (9); $\lambda = \tilde{h}_0/\tilde{R}_0$, initial height aspect ratio with $\tilde{h}_0$ being the initial height of the mixture inside the cylinder and $\tilde{R}_0$ the equivalent radius of the cylinder; V_s, dimensionless settling velocity; L_x, L_y, L_z, dimensions of the computational domain (gravity is along the z-direction); and N_x, N_y, N_z, grid resolution.

Simulation	Shape	Re	λ	V_s	Domain size $L_x \times L_y \times L_z$	Grid resolution $N_x \times N_y \times N_z$
1	C	8430	2	0.020	$12 \times 12 \times 1$	$640 \times 640 \times 159$
2	RR	8430	2	0.020	$10 \times 15 \times 1$	$534 \times 800 \times 159$
3	RR[a]	8430	2	0.020	$10 \times 15 \times 1$	$534 \times 800 \times 159$

[a]The initial concentration field is randomly perturbed.

fluctuations in the current at the time of release. In Sim 2, the current is "ideally" placed in contact with the ambient fluid at the start of the simulation, i.e., no perturbation is artificially added. Since it is difficult to impose some large-scale, organized initial perturbation on the velocity field, the perturbation field in the experiments being unknown, we add a small random perturbation to the density field in Sim 3, in order to crudely approximate the possible presence of initial perturbation in the system.

B. Flow structure

In Figure 16, we present an isometric view of the shape and structure of the current at three time instances, namely, $t = 2.5$, 8.5, and 18.5. The last two time instances are chosen close to the critical times $t_c \approx 9$ and 18 displayed in Figure 7 and discussed in Sec. II C 2, so that one may see the structure of the current at these specific times. The current is materialized through multiple semi-transparent iso-surfaces of the particle phase concentration in the range $0.01 \leq \rho \leq 0.25$. At the bottom of each figure and for each time instance, we show the corresponding distribution of the particle phase concentration in the symmetry $y = 0$ plane. A scale bar of unit dimensionless length (equivalent to 93 mm) is shown in the isometric view. The current initially spreads radially outwards at nearly the same rate in all directions, maintaining its initial rounded rectangular shape. At $t = 2.5$, the majority of the particle-laden mixture is observed to accumulate in an outer elliptical-shaped ring, where the width (normal to the front direction) and height of the ring are not uniform along the current's circumference. The front is thicker and wider along the x-axis compared to the y-axis. At $t = 8.5$, the current still has the shape of an elliptical ring, the major and minor axes of the ring however have rotated by 90° each. The current has thus switched axes. At this time, the azimuthal disparity along the front is readily identified. The current is significantly thicker and more turbulent along the x-axis and becomes progressively thinner and less turbulent as we move towards the initial major y-axis of the RR. At $t = 18.5$, over 90% of particles have settled out of the flow, and the vast majority (~95%) of the remaining suspended particles are confined within two symmetric 90° wedges centred on the positive and negative x-axis.

C. Front evolution and Reynolds number

As a first verification, we compare in Figure 17 the time evolution of the front position for the circular case measured in Exp 10 and predicted in Sim 1. As for the simulation, we compute the front position using two methods. In the first method, the front is taken as the location where the height of the current drops below a critical threshold value ε. The height of the current is calculated by vertically integrating the concentration field between the bottom and top boundaries of the domain as

$$h = \int_0^1 \rho dz. \tag{18}$$

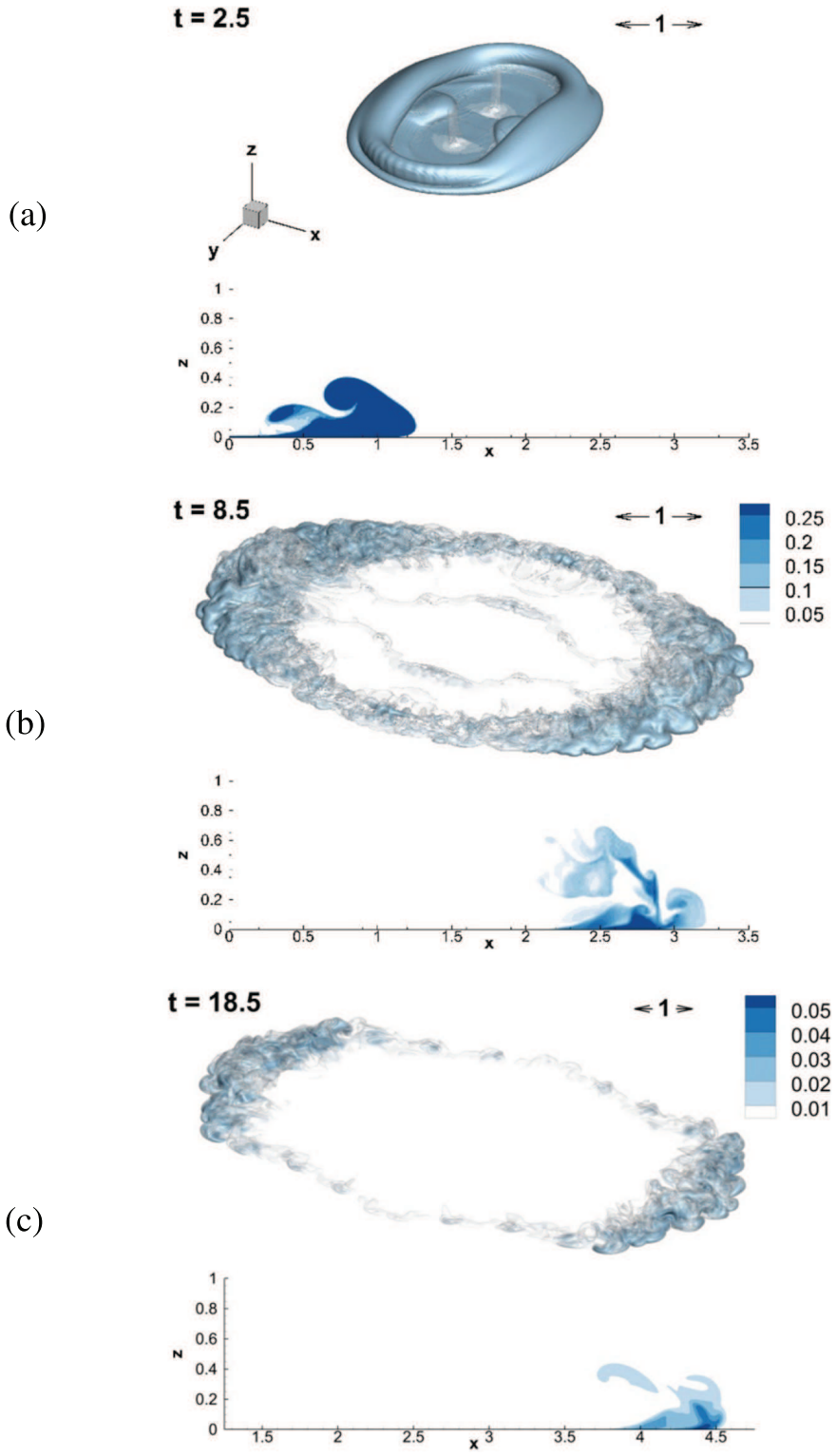

FIG. 16. Structure of the RR release visualized with semi-transparent iso-surfaces of the particle phase concentration (Sim 2). The corresponding distribution of the particle phase concentration in the $y = 0$ plane is shown at the bottom of each frame. The current is thicker, advances faster, and is more turbulent along the x-axis. At $t = 2.5$, the major axis of the RR is oriented along the y-axis, whereas at $t = 8.5$ and 18.5, the major axis of the RR is oriented along the x-axis. The current has switched axes. The corresponding local front Reynolds number along the x-axis and y-axis is (a) 1615 and 322, (b) 173 and 31, and (c) 10 and 0.3, approximately.

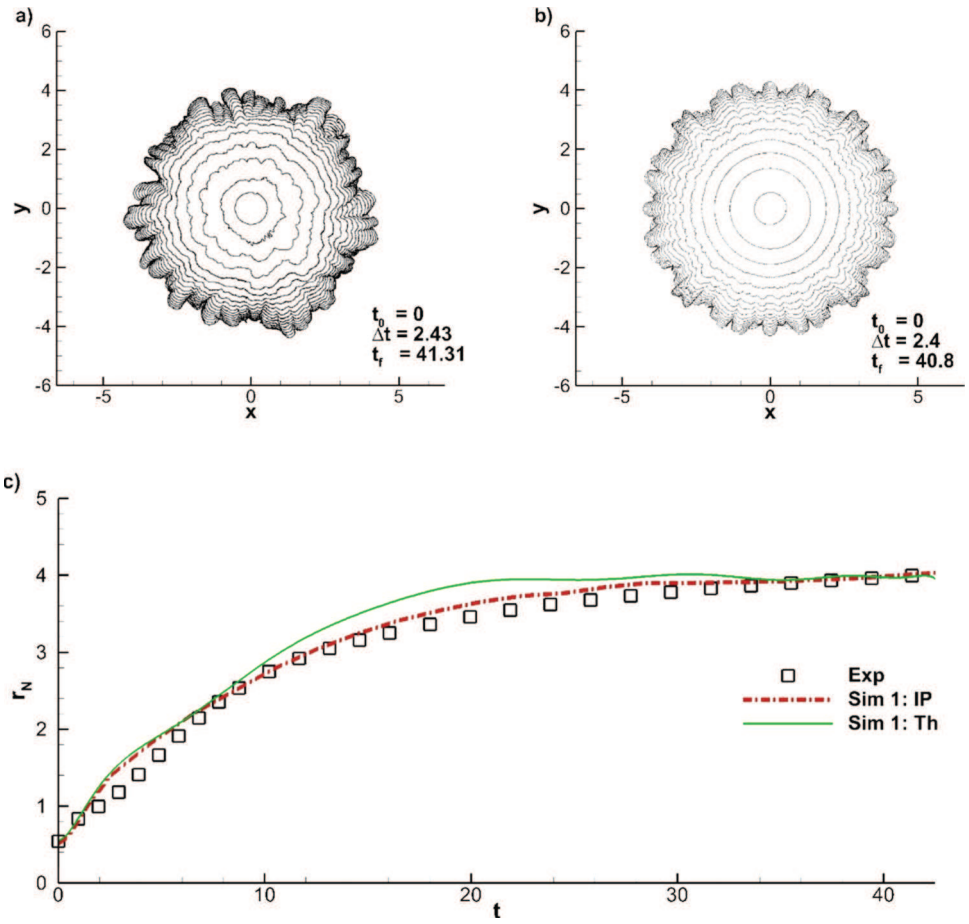

FIG. 17. Temporal evolution of the front of a circular turbidity current: (a) Exp 10; (b) Sim 1. The contours are plotted from $t = t_0$ to $t = t_f$ by steps of Δt. (c) Azimuthally averaged radial location of the front versus time for Exp 10 (symbols) and Sim 1 (solid line: threshold; dashed-dotted line: inflection point method). The relatively high concentration of contours in (a) and (b) and the flattening of the curve in (c) (around $t \approx 14$) mark the onset of the viscous-buoyancy dominated flow regime. All units are dimensionless.

Here, we choose the threshold value to be $\varepsilon = 10^{-4}$. Note that the location of the front is not sensitive to the value of ε in the range $10^{-5} < \varepsilon < 10^{-3}$. This is a common approach in the literature, here referred to as the "threshold method" denoted by (Th). An alternative method for computing the front position has been recently proposed by Ref. 32 and consists of first computing the maximum particle phase concentration ρ_m in the vertical z-direction of the azimuthally averaged particle phase concentration field as

$$\rho_m(r,t) = \max_{z\in[0,1]} \left\{ \frac{1}{2\pi} \int_0^{2\pi} \rho(r,\theta,z,t) d\theta \right\}. \tag{19}$$

ρ_m take values close to 1 within the current and sharply drop to zero beyond the current/ambient interface. Recall that a dimensionless value of 1 corresponds to the initial mixture density of the current and a value of 0 corresponds to the absence of particles. For each time instance t_n, the position of the front is marked as the radial location of the inflection point of a cubic spline curve fit to $\rho_m(r,t_n)$. This method allows for subgrid resolution of the front position without the need of a small threshold value. We refer to this approach as the "inflection point method" denoted by (IP).

As shown in Figure 17(c), the simulation captures well the dynamics of the cylindrical particle-laden current both qualitatively and quantitatively, as indicated by the azimuthally averaged front position which is in good agreement with experimental data. Note that the inflection point method

provides a slightly better agreement with experiments in the intermediate and late stages of the current ($t \geq 8$).

In Figure 18, we present the time evolution of an initially rounded-rectangular turbidity current, obtained from experiment and simulation. As for the simulation, two cases are shown (Sims 2 and 3) the difference being that an initial random perturbation of 5% in the particle phase concentration field was imposed in the latter (see the discussion in Sec. III A). Both simulations are in good agreement with experimental data at early times, namely, $t \leq 14$ (see, e.g., Figure 18(d)). During this stage, the front contours are roughly similar in the simulations. Note that in Figure 18(d), we track the front along the major and minor axes of the RR-current. The front along these axes was calculated by averaging the radial distances (along the positive and negative axes) bounded by a circular wedge centred along each axis with a half-wedge angle of 2.5°. For $t > 14$ (respectively, $t > 24$), the computed front of the Sim 2 (respectively, Sim 3)-current begins to gradually deviate from the experimental one, with the front from the Sim 3-current providing a better match (than the Sim 2-current) to that observed in the experiments. The difference in the computed front location from the Sim 2- and Sim 3-current indicates that the initial perturbation does influence, even though slightly, the dynamics of the simulated currents. As observed in Figure 18(c), the initial perturbation increases the three-dimensionality of the flow and results in a slower moving averaged front.

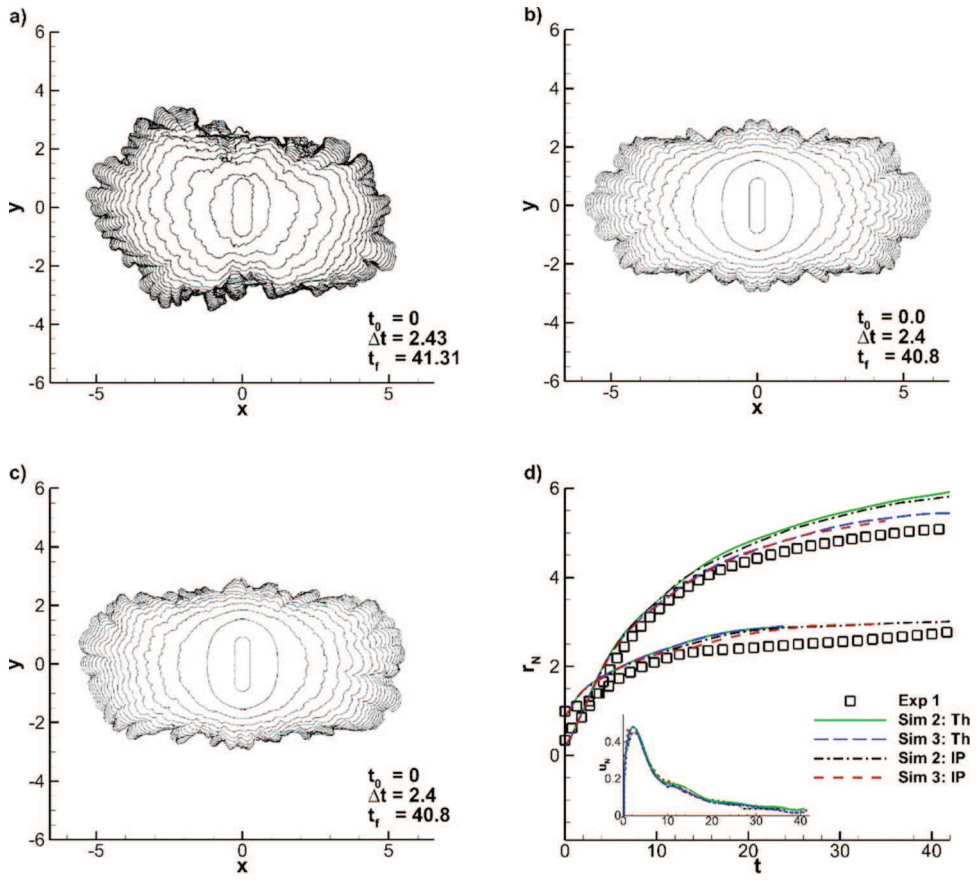

FIG. 18. Temporal evolution of the front of an initially rounded-rectangular turbidity current: (a) Exp 1; (b) Sim 2; and (c) Sim 3. The contours are plotted from a dimensionless time of $t = t_0$ to $t = t_f$ by steps of Δt. (d) Front position versus time for Exp 1 (symbols), Sim 2 (solid line: threshold method; dashed-dotted line: inflection point method), and Sim 3 (long dashed line: threshold method; dashed line: inflection point method). For $t > 24$, the current's thickness along the major axis for Sims 2 and 3 drops below the critical value $\varepsilon = 10^{-4}$. Inset: corresponding dimensionless front velocity along the minor axis. The relatively high concentration of contours in (a)–(c) and the flattening of the r_N-vs-t curve in (d) mark the onset of the viscous-buoyancy dominated flow regime. The dimensionless times for the transition to the viscous regime are approximately $t = 9$ and $t = 18$ for the slow and fast fronts, respectively.

The fact that the computed current for which an initially perturbed particle phase concentration field was applied spreads slower than the unperturbed one may be interpreted as follows. Let us consider the front velocity of the gravity current to be given by the Huppert-Simpson (HS) relation,[33]

$$\tilde{v}_N = Fr\sqrt{\tilde{g}_r\tilde{\eta}_N}, \tag{20}$$

where $\tilde{v}_N$, $\tilde{\eta}_N$, $\tilde{g}_r$, and Fr represent the front velocity, front height, reduced gravity, and the HS Froude number, respectively. During the late stages of the release, the ratio of the current height to ambient height is small and the Froude number may be considered as a constant $Fr = 1.19$. Moreover, assuming the reduced gravity $\tilde{g}_r$ to be constant and expressing the circumferential variation of current height $\tilde{\eta}_N$ as the sum of a mean $\bar{\eta}$ and fluctuating contribution η', we can write

$$\tilde{v}_N = Fr\sqrt{\tilde{g}_r(\bar{\eta} + \eta')}. \tag{21}$$

In (21), we have assumed that the HS relation is applicable at every point along the front of the current. Now applying the azimuthal averaging operator to (21), we can write

$$\tilde{v}_N = Fr\sqrt{\tilde{g}_r\bar{\eta}}\,\overline{\sqrt{\left(1 + \frac{\eta'}{\bar{\eta}}\right)}}. \tag{22}$$

Equation (22) can be expanded in Taylor series of the small perturbation η' and, neglecting terms of $O(\eta'/\bar{\eta})^4$, one obtains

$$\bar{v}_N \approx Fr\sqrt{\tilde{g}_r\bar{\eta}}\left(1 - \frac{1}{8}\frac{\overline{\eta'^2}}{\bar{\eta}^2}\right). \tag{23}$$

Recall that the overbar denotes the azimuthal averaging operator. Note that $Fr\sqrt{\tilde{g}_r\bar{\eta}}$ would be the front velocity if the current was of uniform height. Equation (23) indicates that the larger the ratio of height fluctuations to mean height, the smaller the mean velocity. During the early stages of the release, the mean height of the current is large and therefore, the fluctuations do not significantly affect the front velocity; however, as the mean front height diminishes, $\overline{\eta'^2}/\bar{\eta}^2$ increases and can lead to a slower moving front as observed in Figure 18(d).

The reduced front speed in Sim 3 can also be explained in terms of enhanced entrainment of low-velocity ambient fluid, which must be accelerated by the particle-laden flow resulting in a slower moving current. To investigate this possibility, we monitor the height of the current at the front h_{CM}, defined as twice the centre of mass,[32]

$$h_{CM} = \frac{2\int_0^{L_z}\rho z dz}{\int_0^{L_z}\rho dz}. \tag{24}$$

From the temporal evolution of h_{CM} at the fast front (not shown here), we observe a small difference between Sim 2 and Sim 3 throughout the entire simulation. Moreover, we observe the value of h_{CM} computed from Sim 2 (as compared to Sim 3) to be larger at early times and smaller at later times. The small difference in the values of h_{CM} from both simulations and the change of sign of $(h_{CM,Sim2} - h_{CM,Sim3})$ over time makes it difficult to precisely verify that the perturbed release entrains more ambient fluid. Perhaps a situation with a more substantial initial perturbation, or where the signal-to-noise ratio is larger than the present case can shed light on the validity of (23) and the mechanism of the increased entrainment.

Another possible reason for the discrepancy between simulations and experiments is that in the simulations, we consider truly monodisperse particles of uniform density by imposing a unique settling velocity. In the experiments, however, the size distribution of particles is not exactly monodisperse. This polydispersity of particles may affect the settling velocity leading to further variations in the volume fraction of particles inside the current and consequently modify the reduced gravity and mean front velocity. It is also likely that the particles are not uniformly distributed within the hollow cylinder and some stratification may have occurred before the release, despite our best efforts to have a uniform distribution.

Due to the finite nature of the release and continued deposition, the flow does not remain high-Re number for long. In fact, the Reynolds number Re shown in Table I is analogous to a Grashof or Galileo number[23] and denotes the maximum attainable value which may not be representative of the local Reynolds number experienced by the flow. A local front Reynolds number Re_N may be calculated however from the simulation data. Here, we define it as

$$Re_N(\theta,t) = \frac{u_N h_N}{\tilde{\nu}} \tilde{U}\tilde{L}, \tag{25}$$

where h_N denotes the maximum dimensionless height, as defined in (18), in the head of the current and u_N represents the dimensionless front velocity obtained from the time derivative of the front location. Recall that $\tilde{U}$ and $\tilde{L}$ are the dimensional velocity and length scales of the simulation, respectively, and $\tilde{\nu}$ is the dimensional kinematic viscosity of the interstitial fluid.

In the case of the circular release, u_N and h_N are mostly functions of time (weak spatial dependence) and it is reasonable to assume that Re_N varies only temporally. On the other hand, for the RR release, u_N and h_N additionally depend on the azimuthal location θ along the front and as a result the front Reynolds number is a function of θ and time. Figure 19 shows the evolution of Re_N for the circular (Sim 1) and RR (Sim 2) releases. The blue dashed-dotted line corresponds to the circular release and is denoted in the figure by Re_C, whereas the red solid and green dashed lines correspond to the fast (denoted by Re_F) and slow (denoted by Re_S) axes of the RR, respectively. Re_N corresponds to the local front Reynolds number in the head of the current and its value is therefore only meaningful after about 1 dimensionless time unit needed for the head to form.

Figures 17–19 may be used to establish the transition from the inertia-buoyancy regime to the viscous-buoyancy regime. Initially, just after the head of the gravity current develops around $t = 1.5$, the value of Re_N for the circular and RR releases is of order $O(10^3)$. In the case of the RR release, the magnitude of Re_N decreases with time at different rates along the front. For the slow front, Re_N drops by about two orders of magnitude to a value of $Re_N \approx 20$ by $t = 10$, which approximately corresponds to the flattening of the $r_N(t)$-curve in Figure 18(d) and the close packing of contours along the y-axis in Figure 18(a). On the other hand, the same is observed along the fast front (x-axis) at a later time $t \approx 18$ for which Re_N has dropped to a value of $Re_N \approx 10$. For the circular release (Figure 17), the flattening of the $r_N(t)$-curve occurs around $t = 14$, which corresponds to a value of $Re_N \approx 15$. Based on the above observations, it can be conjectured that a critical value of the local front Reynolds number $Re_{cr} \sim O(10)$ marks the transition from the inertia-buoyancy to the viscous-buoyancy regime.

D. Particle deposition

Iso-contours of the local deposition thickness h_d of a circular and non-circular turbidity current are plotted in Figure 20. Clearly, the deposition pattern strongly depends on the shape of release. The cylindrical release exhibits a roughly circular sedimentation profile (Figures 20(a) and 20(c))

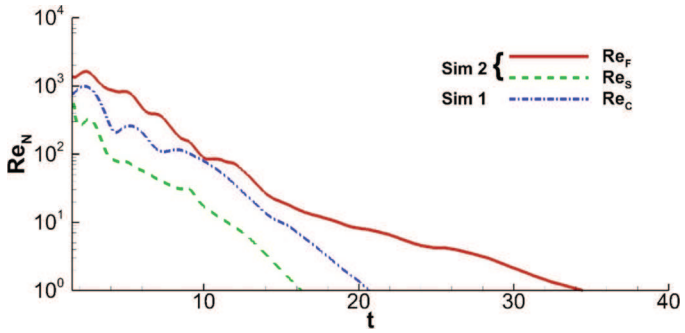

FIG. 19. Local front Re_N number (see text for definition) as a function of time for the RR (Sim 2) and circular (Sim 1) releases. The red solid and green dashed lines correspond to the fast and slow axes of the RR and the blue dashed-dotted line corresponds to the circular release.

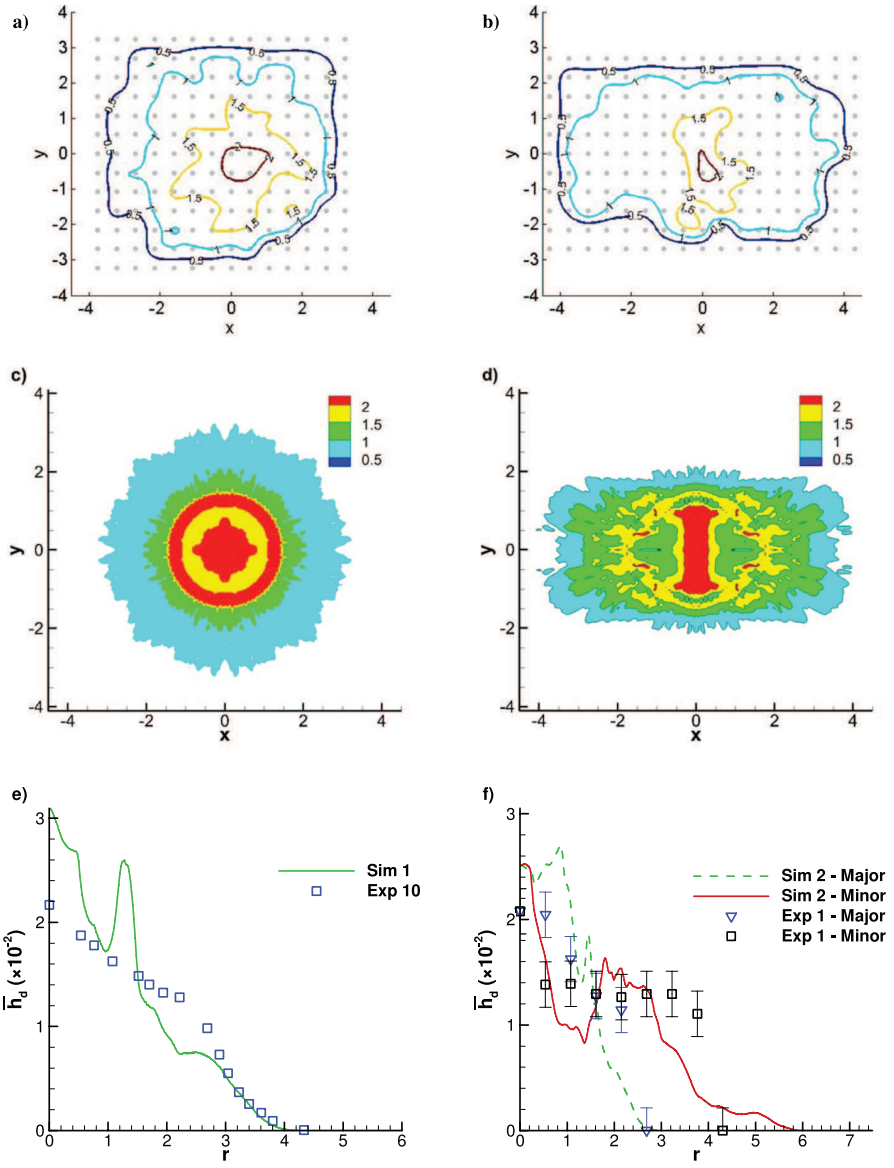

FIG. 20. Contours of the dimensionless thickness of the deposit multiplied by 100 for (a) Exp 10, (b) Exp 1, (c) Sim 1, and (d) Sim 2. The circular marks in the background of (a) and (b) indicate the locations at which measurements were recorded. (e) Azimuthally averaged deposition profile versus radial location from Exp 10 (symbols) and Sim 1 (line). (f) Dimensionless thickness of the deposit along the major and minor axes from Exp 1 (symbols) and Sim 2 (lines).

while that of the RR-release is of rectangular shape, the longer side being along the x-axis (contrary to the initial orientation of the rounded rectangle), the extent of the deposit being well captured in the simulations (Figure 20(d)). Note that in the experiments, the deposit is thickest at the centre of the domain and decreases as one moves radially outwards, whereas in the simulations, a second local maximum is observed at $r \approx 1.3$ for the circular release and at $1.5 \leq r \leq 2$ for the RR release, the specific location being azimuthally dependent. The possible reason for this discrepancy is discussed later.

The mean final deposition thickness $\bar{h}_d$ obtained from the experiment is compared with simulation results in Figures 20(e) and 20(f) for the circular and RR release, respectively. As for the circular release, the numerical deposition thickness is overpredicted (underpredicted) close to the centre (at intermediate radial distances $1.8 < r < 2.8$) and is in good agreement with experiment at larger radial values ($r > 3$). Recall that a local peak at $r \approx 1.3$ is visible in the numerical

deposition thickness as opposed to the experimental one. For the RR release, a roughly similar trend is observed; however, comparison is more difficult since the final thickness is not azimuthally averaged as in the circular case.

In order to understand the presence of the second local maximum of deposition thickness in the simulation, we present in Figure 21 the space-time diagram of the azimuthally averaged height

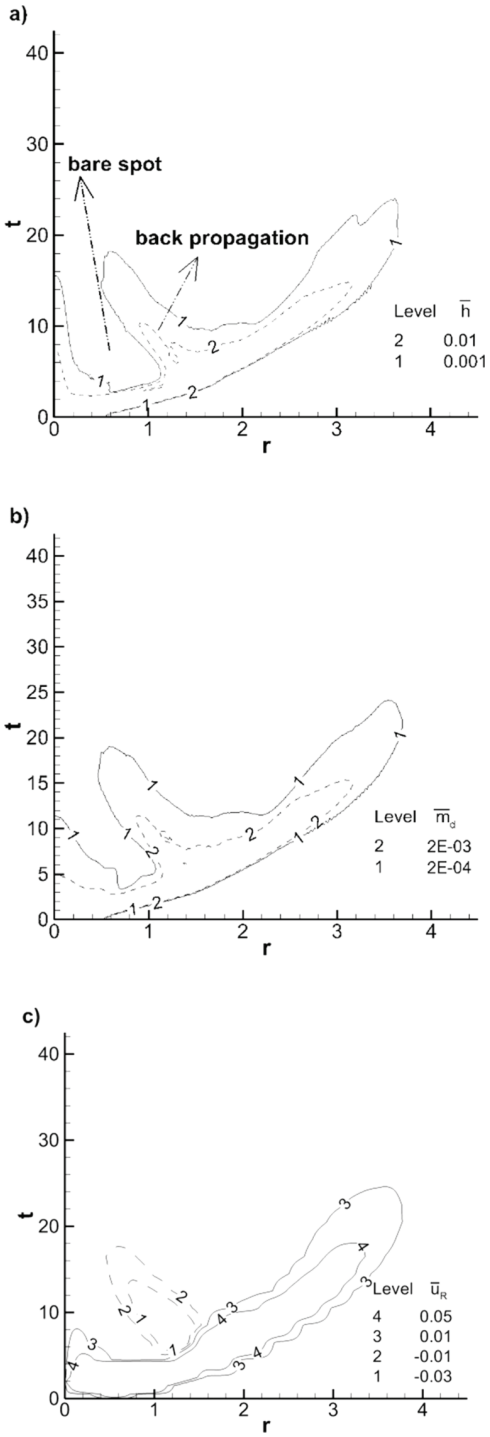

FIG. 21. Contours in space and time of the azimuthally averaged (a) height, (b) mass deposition rate of particles per unit area, and (c) depth-averaged radial velocity of the current for Sim 1. Flow reversal is first observed around $r = 1.2$ and $t = 4.5$.

$\bar{h}$, mass deposition rate of particles per unit area $\bar{m}_d$, and depth-averaged radial velocity inside the current $\bar{u}_r$ of the cylindrical release. Here, $\bar{h}$, $\bar{m}_d$, and $\bar{u}_r$ are computed as

$$\bar{h}(r,t) = \frac{1}{2\pi}\int_0^{2\pi} h(r,\theta,t)d\theta, \qquad \bar{m}_d(r,t) = \frac{V_s}{2\pi}\int_0^{2\pi} \rho(r,\theta,z=0,t)d\theta,$$
$$\bar{u}(r,t) = \frac{1}{2\pi}\int_0^{2\pi} \frac{\int_0^{L_z} \rho(r,\theta,z,t)u_r(r,\theta,z,t)dz}{\int_0^{L_z} \rho(r,\theta,z,t)dz} d\theta. \tag{26}$$

As the material spreads radially outwards, the particle-laden mixture (after about 3.5 dimensionless time units) accumulates in an outer ring and the current takes on the shape of an annulus whose width may be inferred from Figures 16 and 21. The inner boundary of the annulus advances radially outwards up to a time of ≈4.5, at which point the width of the annulus is $\Delta r \approx 0.7$ extending from $r_i \approx 1.2$ to $r_o \approx 1.9$, where r_i and r_o correspond to the inner and outer radii of the annulus. Beyond $t \approx 3.5$, the bare region of negligible current height that forms in the interior of the annulus creates an adverse pressure gradient that acts to slow the advancing current. At $t \approx 4.5$, we observe the inner radius (r_i) of the annulus to advance radially inwards ($dr_i/dt < 0$) indicating reverse flow due to the adverse pressure gradient. This reverse flow is clear in Figure 21(c) where $\bar{u}_r$ is plotted. In this figure, a region of negative radial velocity is observed. This flow reversal seems to be correlated to the location of the second maximum of deposition as observed from the comparison of $\bar{h}$ and the mass deposition rate of particles in Figures 21(a) and 21(b), respectively. A similar flow reversal is observed for the RR release (not shown) and is likely to be responsible for the second maximum in the deposition profiles.

E. Mechanism for the switching of axes

Here, we discuss a possible mechanism for the axes switching. The mechanism lies in the different nature of spreading on the original broad side and the short side of the RR. It has been recently shown[21,22] that in case of a RR release of saline current, the front separates into a fast and a slow moving segment. As described in the Introduction section, the proposed underlying mechanism for such a dynamics is an initial partitioning of the initial release into local volumes during the acceleration and early part of the slumping phases; these local volumes (almost) independently propagate along the direction locally normal to the front. In the present context of a non-axisymmetric particle-laden release, we conjecture that these processes are likely to play a role as well since at early times the density of the mixture is homogeneous and sedimentation is expected to be marginal. It turns out that, at early times, the front velocity for non-circular particle-laden currents are identical to those for saline currents, as shown in Figure 7.

The underlying assumption for the occurrence of the switching of axes in turbidity currents is that the characteristic time scale of sedimentation T_s is much larger than that of the initial partitioning T_i. Since the initial partitioning of the current occurs during the early acceleration phase which lasts about one or two dimensionless time units (see, e.g., the inset in Figure 18(d)), one can estimate the dimensionless time T_i as $T_i \approx 1$. Additionally, one may estimate the characteristic sedimentation time T_s as the time for the particles to cross the characteristic height $\tilde{h}_0$ at a velocity $\tilde{V}_s$. In dimensionless form, this reads $T_s \approx 1/V_s$. Overall, we expect the switching of axes to occur if $T_s/T_i >> 1$, i.e., $V_s << 1$ which is the case in the present work.

F. Possible contribution of bedload transport

The discrepancy between the experimental and numerical deposition profiles may be due to either the redistribution of particles as a result of local bedload transport or possible near-wall particle resuspension. Recall that bedload transport is not accounted for in the present simulations. However, if the flow is energetic and the near-wall shear stress exceeds a critical value, particles may roll or slide over the bed or even be reentrained back into the current. Since the pioneering work of Shields,[34] it is widely accepted that for a near-bed Reynolds number Re_*, there exists a critical shear stress $\tilde{\tau}_{cr}$ above which particles are set in motion (these quantities are defined in

(27)). The value of the critical shear stress depends on several parameters including the particle and fluid densities, the particle diameter, as well as the kinematic viscosity of the fluid. For the present experimental conditions, we estimate the critical shear stress to be $\tilde{\tau}_{cr} \approx 0.016\ \mathrm{N/m^2}$ and the corresponding near-bed critical Reynolds number $Re_* \approx 1.2$, using

$$\tilde{\tau}_{cr} = (\tilde{\rho}_p - \tilde{\rho}_a)\tilde{g}\tilde{d}_p\theta_{cr}, \qquad Re_* = \frac{\sqrt{\tilde{\tau}_{cr}/\tilde{\rho}_a}\tilde{d}_p}{\tilde{\nu}}, \tag{27}$$

where θ_{cr} is the so-called critical Shields parameter which depends on Re_* and is here estimated as $\theta_{cr} \approx 0.1$ using the Shields diagram.

In order to assess the possible contribution of bedload transport, we plot in Figures 22(a) and 22(b) the space-time diagram of the azimuthally averaged vertical gradient $\overline{du_r/dz}$ of the radial velocity at the bottom wall for the circular release. Note that a value of the critical shear stress $\tilde{\tau}_{cr} \approx 0.016\ \mathrm{N/m^2}$ corresponds to $\left|\overline{du_r/dz}\right| \approx 13$. A positive (respectively, negative) velocity gradient above this value is likely to indicate outward (respectively, inward) bedload transport. In Figure 22, only the regions of $\left|\overline{du_r/dz}\right| > 13$ are mapped. The wall shear stress is observed to be predominantly positive and above the threshold in a significant region of the space-time diagram (Figure 22(a)). According to this criterion, possible outward bedload transport is likely to be present. Note that some small regions of significantly negative wall shear stress are also visible, for instance, at $(r \approx 1, t \approx 2.5)$ as seen in Figure 22(b). Interestingly, this region is observed to be at the vicinity of a region of significantly positive wall shear stress located at $(r \approx 0.5, t \approx 2.5)$ approximately. This may lead to bedload transport in such a way that particles accumulate at some specific radial location. This is in line with the observation of a second local maximum of the mean deposition thickness of the circular release, the location of which being at $r \approx 1.3$ (Figure 20(e)).

As for the RR-release, the mean quantities $\overline{d\mathrm{u}/dz}$ and $\overline{d\mathrm{v}/dz}$ corresponding to the vertical velocity gradient at the bottom wall along the minor x-axis and major y-axis are plotted in Figures 22(c)-22(f). The overbar here denotes the following averaging:

$$\begin{aligned}
\overline{d\mathrm{u}/dz}\,(x,0,0,t) &= \frac{1}{2}[d\mathrm{u}/dz\,(x,0,0,t) - d\mathrm{u}/dz\,(-x,0,0,t)], \\
\overline{d\mathrm{v}/dz}\,(0,y,0,t) &= \frac{1}{2}[d\mathrm{v}/dz\,(0,y,0,t) - d\mathrm{v}/dz\,(0,-y,0,t)],
\end{aligned} \tag{28}$$

where u and v are the velocity components in the x- and y-directions, respectively. Again a significant (respectively, small) region of highly positive (respectively, negative) wall shear stress is observed, suggesting the possible contribution of bedload transport to be significant. Note that in this non-circular release, the wall shear stress is different between the x- and y-directions, both in terms of distribution and intensity. This is in line with the highly non-axisymmetric spatial distribution of the deposition thickness observed in Figures 20(b) and 20(d).

Figure 23 presents the radial distribution of $\overline{du_r/dz}$ at two time instances $t = 2$ and $t = 2.5$, respectively, in the case of the circular release. Three regimes are defined depending on the specific value of $\overline{du_r/dz}$, namely, a region of no-bedload transport ($-13 \leq \overline{du_r/dz} \leq 13$), possible outward transport ($\overline{du_r/dz} > 13$), and possible inward transport ($\overline{du_r/dz} < -13$). Strong fluctuations of the bottom shear stress are observed. For instance, at the time $t = 2.5$, $\overline{du_r/dz} \approx 220$ at $r \approx 0.6$ while $\overline{du_r/dz} \approx -150$ at $r \approx 0.75$. In addition, the local wall shear stress appears to be highly time-dependent, since the aforementioned fluctuation is not visible at time $t = 2$, for instance.

Iso-contours of the particle phase concentration and zones of high vorticity are plotted in Figure 24 for the same time instances as in Figure 23. Here, regions of high vorticity are obtained from contours of the swirling strength λ_{ci} which is defined as the absolute value of the imaginary part of the complex eigenvalue of the velocity gradient tensor.[35,36] Considering Figure 23 together with Figure 24, one may observe that the positive and negative peaks of $\overline{du_r/dz}$ are strongly correlated with the regions of high vorticity. In particular, the peak of positive (respectively, negative) shear stress is found to correspond to the presence of a counter-clockwise (respectively, clockwise) rotating vortex tube that is generated close to the bottom wall. For example, at $t = 2$, the negative peak observed at $r \approx 1.1$ in Figure 23 corresponds to the clockwise rotating vortex tube denoted as V_{1a} in Figure 24(a) and located at $(r \approx 1.1, z \approx 0.05)$.

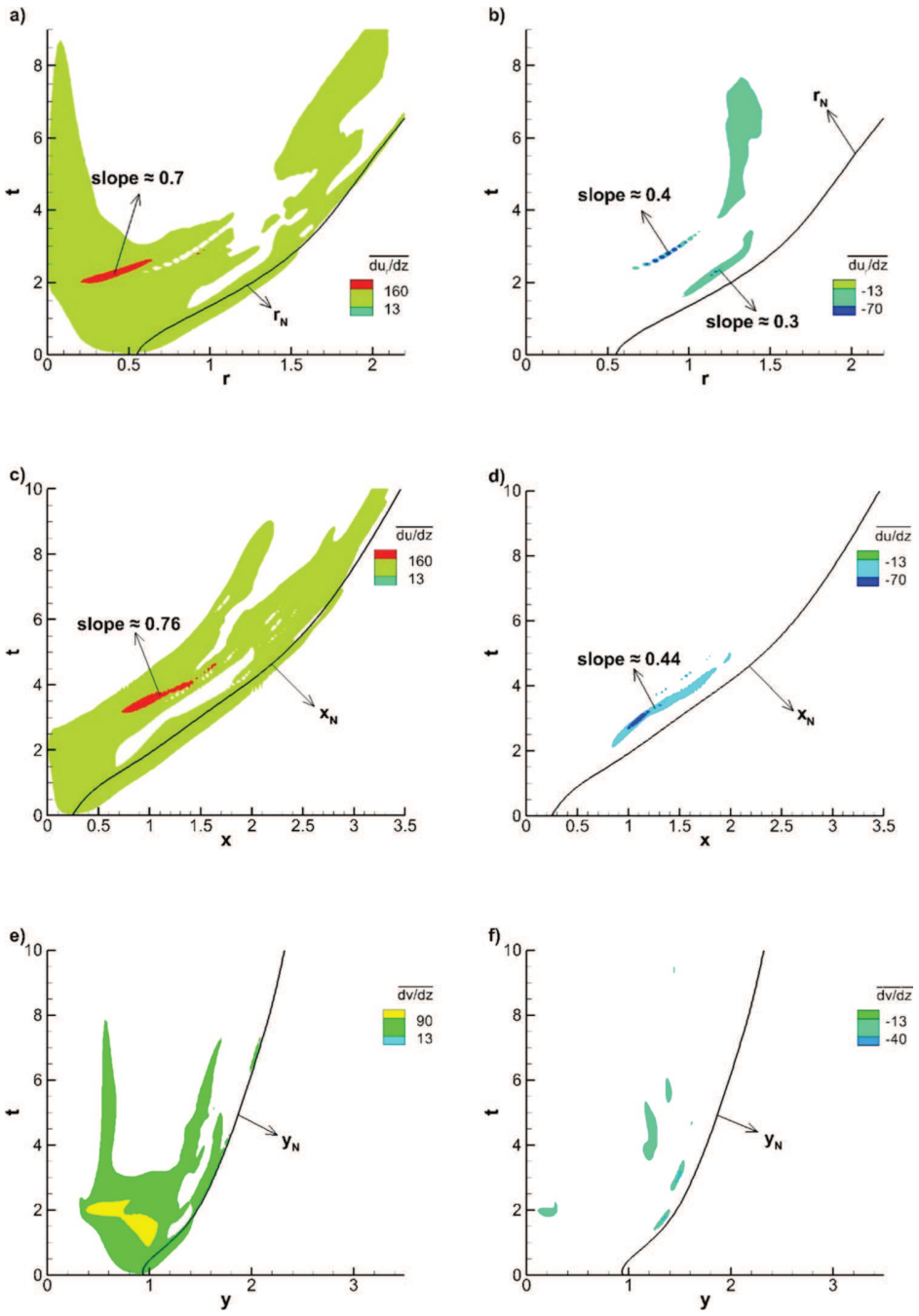

FIG. 22. Contours in time and space of the azimuthally averaged, vertical gradient of the radial component of velocity on the wall (wall shear stress) for Sim 1: (a) positive contours and (b) negative contours. Contours in time and space of the vertical velocity gradient on the wall along the minor (x) axis of the RR for Sim 2: (c) positive contours and (d) negative contours. Contours in time and space of the vertical velocity gradient on the wall along the major (y) axis of the RR for Sim 2: (e) positive contours and (f) negative contours. The slope of peak values is calculated as change in distance divided by change in time. The solid black line in each figure corresponds to the front location (see Figures 17(c) and 18(d)).

G. Possible contribution of particle resuspension

In this section, we aim at assessing the possible effect of particle resuspension on the dynamics and deposition of a particle-laden current. In general, resuspension occurs when the bottom shear stress is large enough to dislodge the particle from the bed and the near-wall vertical velocity

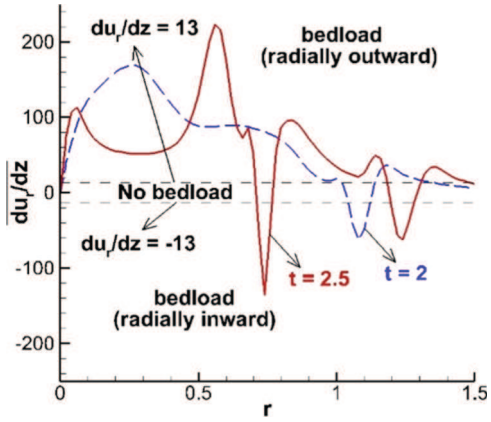

FIG. 23. Snapshots of $\overline{du_r/dz}$ on the wall from Sim 1 at $t = 2$ (dashed line) and $t = 2.5$ (solid line). The thin dashed horizontal lines corresponding to $\overline{du_r/dz} = \pm 13$ separate three regions: (i) no bedload transport ($\left|\overline{du_r/dz}\right| \leq 13$), (ii) potential for radially outward bedload transport ($\overline{du_r/dz} > 13$), and (iii) potential for radially inward bedload transport ($\overline{du_r/dz} < -13$).

exceeds the particle settling velocity. In Figure 24, we plot the radial distribution of the vertical velocity component w at two distances from the bottom wall, namely, $z = 4d_p$ and $2d_p$, respectively. For comparison, the criterion $w = V_s$ is also plotted. Recall that all the variables in Figure 24 are azimuthally averaged. At $t = 2$, one can see at a distance of $z = 2d_p$ from the wall that the vertical velocity never reaches the threshold value $w = V_s$, while for $z = 4d_p$, the region for which $w > V_s$ is marginal. Similarly, at $t = 2.5$, only few $w > V_s$ regions are observed. Overall, the results of Figure 24 support the assumption done in the simulations that the possible contribution of resuspension is small and hence can be neglected.

H. Vortex dynamics

As mentioned earlier, the high values of the bottom shear stress and local vertical velocity w are observed in regions of near-wall vortex tubes. For instance, the vortex tubes V_{1a} and V_{1b} depicted in Figure 24 exhibit a clockwise rotation and hence act to push fluid vertically upward

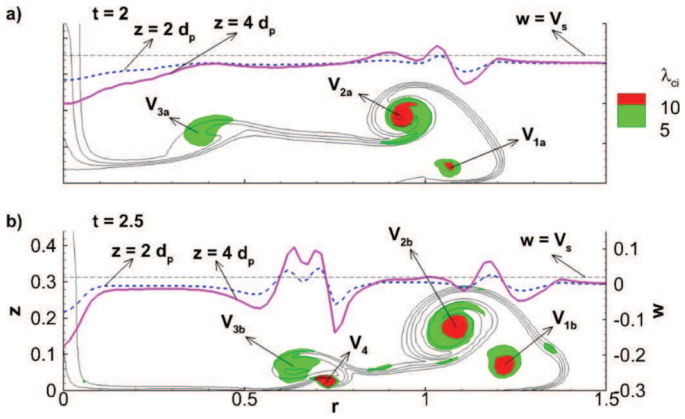

FIG. 24. (a) Snapshot of the current from Sim 1 at $t = 2$. The thin solid lines represent contours of particle phase concentration and mark the location of the current in the r-z plane (all quantities in the figure are azimuthally averaged). Regions of high vorticity are denoted by the vortex tubes: V_{1a}, V_{2a}, and V_{3a}. The thick solid (respectively, dashed) line describes the radial variations in the vertical velocity component w at a distance of $z = 4d_p$ (respectively, $z = 2d_p$) from the bottom wall (in dimensionless terms, $d_p = 3.2 \times 10^{-3}$). Finally, the thin horizontal dashed line corresponds to a critical value of $w = V_s$ above which, particles could lift off and be reentrained by the current. (b) Same as (a) at $t = 2.5$.

(respectively, downward) in the region just behind (respectively, in front of) the centre of the vortex core. This is in line with the positive and negative values of w in the vicinity of V_{1a} and V_{1b}. One can also observe the presence of two counter rotating vortices, namely, V_{3b} (counter-clockwise rotating) and V_4 (clockwise rotating) inside the body of the current (see, e.g., Figure 24(b)) leading to local oscillations in the amplitude of w.

Unlike the bottom shear stress, which remains above the critical value $\left|\overline{du_r/dz}\right| > 13$ over a wide portion of the current's length, the amplitude of the vertical velocity component w is above the critical condition $w > 0.02$ only in some narrow regions of the current. Again, these regions correspond to the presence of intense near-wall vortex structures which move radially outwards at a velocity which is close to that of the current's front. These vortex tubes may grow in size and intensity (V_{1a} vs. V_{1b}), move closer to the bottom wall (V_{3a} vs. V_{3b}), or move away from the bottom wall (V_{1a} vs. V_{1b}). Interestingly, as the counter-clockwise rotating vortex V_{3b} approaches the bottom wall, it locally accelerates the flow near the surface. This local acceleration coupled with the no-slip boundary condition at the bottom wall results in the formation of a clockwise rotating tube V_4.

IV. CONCLUSION

We have presented results from experiments and simulations of circular and non-circular finite-volume Boussinesq density currents, including particle-laden and density-driven (scalar) flows. The initial shape of the release was shown to significantly influence the propagation and deposition of the particles, with a substantial azimuthal dependence for non-circular releases. In particular, the measurements of the time evolution of the front and spatial distributions of the final deposition thickness indicate that for a rounded-rectangular release, the current advances the fastest (respectively, slowest), extends the farthest (respectively, shortest), and deposits the most (respectively, least) amount of particles along its initial shortest (respectively, longest) side, which results in the switching of initial major and minor axes of the release. This switching of axes is a consequence of the initial local volume partitioning of the current similar to that described in Refs. 21 and 22 for saline non-circular currents, since during the early acceleration phase, the switching of axis observed in saline currents is similarly observed in particle-laden currents provided the characteristic time of sedimentation is larger than that of the initial partitioning, which is here verified when $V_s \ll 1$.

Various parameters such as the settling velocity, height aspect ratio, and initial volume fraction of particles in the mixture were varied in order to assess their influence on the dynamics and deposition of non-circular releases and confirm the robustness of the abovementioned dynamics with respect to these parameters.

Fully resolved simulations were performed in order to complement the experiments and provide insight about local processes involved in the deposition of the particles in circular and non-circular releases, in particular, bedload transport and particle resuspension. First, the front speed and deposition pattern compares favourably with experiments; however, slight differences are observed. The thickness at the centre of the deposit is smaller in the experiments than in the simulations and some local extrema in the deposition profile are observed in the simulations contrary to experiments where the measured thickness monotonically decreases as one moves radially outwards.

The spatial and temporal evolution of the near-wall vertical velocity inside the current was considered and suggests that particle resuspension only marginally occurs in the present problem. In particular, the vertical component of the near-wall velocity rarely exceeds the settling velocity and when this occurs it is limited to a small portion of the domain only, supporting the assumption done in the simulations that the contribution of resuspension can be neglected.

A detailed inspection of the spatial and temporal evolution of the wall shear stress inside the current reveals that bedload transport is likely to influence the deposition of particles. More specifically, the wall shear stress is found to be significant (as compared to a critical threshold) over a wide portion of the current's body and for significant times. This effect however is not taken into account in the simulations and may need to be included to confirm if it is responsible for the observed discrepancy between experiments and simulations. Overall, the regions of largest near-wall vertical velocity and wall shear stress were observed to correspond to the location of vorticies. This confirms

that the local structure of the flow inside non-circular particle-laden flows may have a significant influence on the transport and deposition of particles.

Finally, it is worth recalling that the initial Reynolds numbers of the present experiments and simulations were chosen in the range $O(10^4)$ to be representative of turbulent flows as in saline density currents.[29] However, the present results show that the local maximum Reynolds number is of $O(10^3)$ which may indicate that the current is likely to be only turbulent in its earliest stages, the rest probably being transitional (see, e.g., the flow structure in Figure 16). In any case, larger-scale laboratory experiments or simulations are needed to confirm that the present results extend to fully turbulent flows.

ACKNOWLEDGMENTS

This study was supported by the Chateaubriand Fellowship provided by the French Embassy in the USA as well as the National Science Foundation Partnership for International Research and Education (PIRE) Grant (No. NSF OISE-0968313). The experiments were carried out at the Institut de Mécanique des Fluides de Toulouse (IMFT) in Toulouse, France. Some of the computational time was provided by the Scientific Groupment CALMIP (Project No. P1013), the contribution of which is greatly appreciated. We thank Alexis Bougouin for having kindly provided the particle size distribution displayed in Figure 3. The two reviewers are thanked for their excellent and insightful comments which greatly improved the quality of the paper.

[1] J. W. Rottman and J. E. Simpson, "Gravity currents produced by instantaneous releases of a heavy fluid in a rectangular channel," J. Fluid Mech. **135**, 95–110 (1983).
[2] M. A. Hallworth, H. E. Huppert, and M. Ungarish, "Axisymmetric gravity currents in a rotating system: Experimental and numerical investigations," J. Fluid Mech. **447**, 1–29 (2001).
[3] J. E. Simpson, "Gravity currents in the laboratory, atmosphere and ocean," Annu. Rev. Fluid Mech. **14**, 213–234 (1982).
[4] P. H. Kuenen, "Experimental turbidite lamination in a circular flume," J. Geol. **74**, 523–545 (1966).
[5] G. V. Middleton, "Experiments on density and turbidity currents: I. Motion of the head," Can. J. Earth Sci. **3**(4), 523–546 (1966).
[6] R. V. Fisher, "Features of coarse-grained, high-concentration fluids and their deposits," J. Sediment. Petrol. **41**(4), 916–927 (1971).
[7] D. R. Lowe, "Sediment gravity flows: Their classification and some problems of application to natural flows and deposits," SEPM Spec. Publ. **27**, 75–82 (1979).
[8] G. Parker, Y. Fukushima, and H. M. Pantin, "Self-accelerating turbidity currents," J. Fluid Mech. **171**, 145–181 (1986).
[9] T. Maxworthy, "The dynamics of sedimenting surface gravity currents," J. Fluid Mech. **392**, 27–44 (1999).
[10] E. Meiburg and B. Kneller, "Turbidity currents and their deposits," Annu. Rev. Fluid Mech. **42**, 135–156 (2010).
[11] R. T. Bonnecaze, H. E. Huppert, and J. R. Lister, "Particle-driven gravity currents," J. Fluid Mech. **250**, 339–369 (1993).
[12] B. W. Dade and H. E. Huppert, "A box model for non-entraining, suspension-driven gravity surges on horizontal surfaces," Sedimentology **42**, 453–470 (1995).
[13] J. Dufek and G. W. Bergantz, "Suspended load and bed-load transport of particle-laden gravity currents: The role of particle–bed interaction," Theor. Comput. Fluid Dyn. **21**, 119–145 (2007).
[14] H. Lee, M. Y. Ha, and S. Balachandar, "Work-based criterion for particle motion and implication for turbulent bed-load transport," Phys. Fluids **24**, 116604 (2012).
[15] L. Boegman and G. N. Ivey, "Flow separation and resuspension beneath shoaling nonlinear internal waves," J. Geophys. Res., [Oceans] **114**, 1978–2012, doi:10.1029/2007jc004411 (2009).
[16] H. Lee and S. Balachandar, "Critical shear stress for incipient motion of a particle on a rough bed," J. Geophys. Res.: Earth Surf. **117**(F1), F01026, doi:10.1029/2011jf002208 (2012).
[17] C. Gladstone, J. C. Phillips, and R. J. Sparks, "Experiments on bidisperse, constant-volume gravity currents: Propagation and sediment deposition," Sedimentology **45**, 833–844 (1998).
[18] R. T. Bonnecaze, M. A. Hallworth, H. E. Huppert, and J. R. Lister, "Axisymmetric particle-driven gravity currents," J. Fluid Mech. **294**, 93–121 (1995).
[19] M. Ungarish and H. E. Huppert, "The effects of rotation on axisymmetric gravity currents," J. Fluid Mech. **362**, 17–51 (1998).
[20] C. Gladstone and A. W. Woods, "On the application of box models to particle-driven gravity currents," J. Fluid Mech. **416**, 187–195 (2000).
[21] N. Zgheib, T. Bonometti, and S. Balachandar, "Long-lasting effect of initial configuration in gravitational spreading of material fronts," Theor. Comput. Fluid Dyn. **28**, 521–529 (2014).
[22] N. Zgheib, "Gravity currents from non-axisymmetric releases," Doctoral dissertation (Institut National Polytechnique de Toulouse, University of Florida, 2015).
[23] F. Necker, C. Härtel, L. Kleiser, and E. Meiburg, "High-resolution simulations of particle-driven gravity currents," Int. J. Multiphase Flow **28**, 279–300 (2002).
[24] F. Blanchette, M. Strauss, E. Meiburg, B. Kneller, and M. E. Glinsky, "High-resolution numerical simulations of resuspending gravity currents: Conditions for self-sustainment," J. Geophys. Res., [Oceans] **110**, 1978–2012, doi:10.1029/2005jc002927 (2005).

[25] G. D. Scott and D. M. Kilgour, "The density of random close packing of spheres," J. Phys. D: Appl. Phys. **2**(5), 863 (1969).
[26] M. I. Cantero, S. Balachandar, and M. H. García, "An Eulerian–Eulerian model for gravity currents driven by inertial particles," Int. J. Multiphase Flow **34**, 484–501 (2008a).
[27] A. Jackson, B. Turnbull, and R. Munro, "Scaling for lobe and cleft patterns in particle-laden gravity currents," Nonlinear Processes Geophys. **20**(1), 121–130 (2013).
[28] M. I. Cantero, M. H. García, and S. Balachandar, "Effect of particle inertia on the dynamics of depositional particulate density currents," Comput. Geosci. **34**(10), 1307–1318 (2008b).
[29] T. Bonometti and S. Balachandar, "Effect of Schmidt number on the structure and propagation of density currents," Theor. Comput. Fluid Dyn. **22**(5), 341–361 (2008).
[30] T. A. Cortese and S. Balachandar, "High performance spectral simulation of turbulent flows in massively parallel machines with distributed memory," Int. J. High Perform. Comput. Appl. **9**, 187–204 (1995).
[31] M. I. Cantero, S. Balachandar, and G. H. Marcelo, "High-resolution simulations of cylindrical density currents," J. Fluid Mech. **590**, 437–469 (2007).
[32] H. J. Anjum, J. N. Mcelwaine, and C. C. P. Caulfield, "The instantaneous Froude number and depth of unsteady gravity currents," J. Hydraul. Res. **51**(4), 432–445 (2013).
[33] H. E. Huppert and J. E. Simpson, "The slumping of gravity currents," J. Fluid Mech. **99**, 785–799 (1980).
[34] A. Shields, Application of Similarity Principles and Turbulence Research to Bed-Load Movement, translated by W. P. Ott and J. C. Uchelen (Mitt. Preuss. Verschsanst., Berlin, Wasserbau Schiffbau; California Institute of Technology, Pasadena, California, 1936), Report No. 167.
[35] J. Zhou, R. J. Adrian, S. Balachandar, and T. M. Kendall, "Mechanisms for generating coherent packets of hairpin vortices in channel flow," J. Fluid Mech. **387**, 353–396 (1999).
[36] P. Chakraborty, S. Balachandar, and R. J. Adrian, "On the relationships between local vortex identification schemes," J. Fluid Mech. **535**, 189–214 (2005).